Disturbed mitochondrial dynamics in CD8$^+$ TIL reinforce T cell exhaustion

Yi-Ru Yu[1,2,11], Hana Imrichova[3,11], Haiping Wang[1,2], Tung Chao[1,2], Zhengtao Xiao[4], Min Gao[5], Marcela Rincon-Restrepo[1,2], Fabien Franco[1,2], Raphael Genolet[1,2], Wan-Chen Cheng[1,2], Camilla Jandus[1,2], George Coukos[1,2], Yi-Fan Jiang[6], Jason W. Locasale[4], Alfred Zippelius[7,8], Pu-Ste Liu[9], Li Tang[5], Christoph Bock[3,10], Nicola Vannini[1,2], Ping-Chih Ho[1,2]

[1]Department of Oncology, University of Lausanne, Lausanne, Switzerland
[2]Ludwig Institute for Cancer Research, University of Lausanne, Epalinges, Switzerland
[3]CeMM Research Center for Molecular Medicine of the Austrian Academy of Sciences, Vienna, Austria
[4]Department of Pharmacology and Cancer Biology, Duke University School of Medicine, Durham, USA
[5]Institute of Bioengineering, Institute of Materials Science and Engineering, Ecole Polytechnique Fédérale de Lausanne, Lausanne, Switzerland
[6]Graduate Institute of Molecular and Comparative Pathobiology, School of Veterinary Medicine, National Taiwan University, Taipei, Taiwan
[7]Department of Biomedicine, Laboratory Cancer Immunology, University Hospital and University of Basel, Basel, Switzerland
[8]Medical Oncology, University Hospital Basel, Basel, Switzerland
[9]Institute of Cellular and System Medicine, National Health Research Institute, Miaoli County, Taiwan
[10]Department of Laboratory Medicine, Medical University of Vienna, Vienna, Austria
[11]These authors contribute equally to this work

Correspondence:
Ping-Chih Ho
Department of Fundamental Oncology, University of Lausanne,
Chemin des Boveresses 155, 1066 Epalinges, Switzerland
Phone: 41-0-21-692-5947
Fax: 41-0-21-314-7477
Email: ping-chih.ho@unil.ch

Abstract

The metabolic challenges present in tumors attenuate the metabolic fitness and anti-tumor activity of tumor-infiltrating T lymphocytes (TILs). However, it remains unclear whether persistent metabolic insufficiency can imprint permanent T cell dysfunction. We found that TILs accumulated depolarized mitochondria as a result of decreased mitophagy activity and displayed functional, transcriptomic and epigenetic characteristics of terminally exhausted T cells. Mechanistically, reduced mitochondrial fitness in TILs was induced by the coordination of T cell receptor stimulation, microenvironmental stressors and PD-1 signaling. Enforced accumulation of depolarized mitochondria with pharmacological inhibitors induced epigenetic reprogramming toward terminal exhaustion, indicating that mitochondrial deregulation was causal of T cell exhaustion. Furthermore, supplementation with nicotinamide riboside enhanced T cell mitochondrial fitness and improved responsiveness to anti-PD-1 treatment. Together, our results reveal new insights on how mitochondrial dynamics and quality orchestrate T cell anti-tumor responses and commitment to the exhaustion program.

Introduction

Cancer immunotherapy elicits remarkable therapeutic outcomes in cancer patients and has become a paradigm-shifting arsenal for cancer treatment. However, the tumor microenvironment (TME) imposes various regulations to hamper the anti-tumor immunity of infiltrating immune cells[1, 2]. Among these microenvironmental regulations, metabolic restriction has been shown to suppress TIL anti-tumor responses by interfering with transcriptional and translational regulations[3, 4]. However, it remains unexplored how TILs adjust their metabolic programs to cope with sustained metabolic challenges imposed by the TME, and whether the inability to engage proper metabolic adaptation reinforces persistent T cell dysfunction as a result of sustained metabolic insufficiency.

Mitochondrial dynamics, including mitochondria trafficking and remodeling of mitochondrial architecture, mass and activity, are important drivers for sustaining metabolic fitness in response to metabolic perturbations. During nutrient deprivation, increased mitochondrial fusion and biogenesis allow cells to support metabolic demands[5]. However, damaged mitochondria accumulating during this process must be cleaned up by mitophagy. The inability to operate mitophagy results in increased mitochondrial mass associated with reduced mitochondrial membrane potential, a mitochondrial phenotype observed in aged cells[6, 7]. Accumulation of damaged mitochondria further reprogram epigenome and transcriptome via altered retrograde signals that are controlled by metabolites generated from mitochondria and prevent mitochondrial biogenesis[8, 9]. Recently, mitochondrial dynamics have been suggested to modulate generation of memory $CD8^+$ T cells[10, 11] and decreased mitochondrial biogenesis and robust mitochondrial ROS production could promote T cell dysfunction in chronic viral infection and tumors[12, 13, 14]. These studies underscore the importance of mitochondrial function to tailoring T cell immune responses.

Prolonged exposure to antigens induces T cell exhaustion, a special differentiation state characterized by increased expression of co-inhibitory receptors and declined proliferative capacity and production of type I immune cytokines, in tumors and chronic viral infection[15, 16, 17]. T cells with severe exhausted features, referred as terminally exhausted T cells, sustain exhausted characteristics even after antigen withdrawal[18, 19] and are refractory to anti-PD-1 (programmed cell death protein 1) treatment[6, 20]. Terminally exhausted T cells have specialized DNA methylation pattern and chromatin architecture that may lock T cells in a permanently dysfunctional state[21, 22, 23]. Interestingly, a subset of $CD8^+$ T cells expressing the transcription factor T-cell factor 1 (TCF1) display distinct transcriptomic and epigenetic landscapes compared to exhausted T cells[24, 25], and their stem-like phenotype contributes to a proliferative burst upon PD-1 blockade treatment in tumors and chronic viral infection[26, 27, 28, 29]. These findings suggest that TILs may undergo distinct epigenetic reprogramming that dictates the severity of exhaustion and stem-like features. However, the underlying triggers of distinct epigenetic reprogramming in TILs remain unknown.

Results

Tumor-infiltrating CD8$^+$ T cells accumulate dysfunctional mitochondria

To investigate whether CD8$^+$ T cells adjust mitochondrial dynamics and activity to counteract metabolic stresses in the TME, we examined mitochondrial mass and membrane potential in activated CD8$^+$ T cells from spleens, draining lymph nodes (dLNs) and tumors from melanoma-engrafted mice by staining with MitoTracker Green (MG) and MitoTracker Deep Red (MDR), respectively. CD8$^+$ TILs increased mitochondrial mass and membrane potential compared to T cells in spleens and dLNs, as reported in human renal cell carcinomas (**Fig. 1a,b**)[14]. We also observed similar mitochondrial features in the genetically engineered murine melanoma model (referred as Braf/Pten mice) (**Extended Data Fig. 1a-c**)[30]. However, the ratio of MDR to MG, an indication of mitochondrial activity per mitochondrial mass[31], was decreased in TILs, suggesting that TILs might fail to fully utilize mitochondrial activity (**Figure 1c** and **Extended Data Figure 1d**). Despite electron microscopy confirmed that TILs possessed more mitochondria compared to splenic T cells, we found that TILs contained lower copy numbers of mitochondrial DNA (mtDNA) (**Figure 1d-f**), suggesting that mitochondrial quality in TILs might be compromised. Importantly, mitochondria in TILs exhibited damaged phenotypes, including disrupted membrane structures, cristae structure, and declined cristae number and length of crista per mitochondrion (**Figure 1g-i**), implying that TILs contain poor quality mitochondria. Moreover, we found that mitochondria in TILs displayed a physically close ultrastructure with reduced crista volume in a 3D-reconstructed electron microscopy analysis (**Figure 1j-l**), indicating that mitochondria may undergo certain dynamic changes to compensate for their insufficiency of mitochondrial activity. We also found that mitochondria-associated membrane (MAM), which can be induced by mitochondrial stress signal[32], was increased in TILs (**Figure 1m**). Mitochondrial reactive oxygen species (mtROS) was elevated in TILs, whereas intracellular ROS remained similar between T cells from spleens and tumors (**Figure 1n-o** and **Extended Data Figure 1e**). Collectively, these data reveal that CD8$^+$ T cells are prone to accumulating mitochondria with compromised mitochondrial membrane potentials in the TME.

Mitophagy defect forces accumulation of depolarized mitochondria

Intriguingly, we found that CD8$^+$ TILs contained two major subsets with distinct mitochondrial morphology: one subset had relatively normal mitochondrial morphology accompanied by autophagosome-like vesicles in the cytoplasm, whereas the other subset of TILs possessed disrupted cristae (**Extended Data Figure 2a**). This heterogeneity in CD8$^+$ TILs was also observed by examining the ratio of MDR to MG. CD8$^+$ T cells displayed higher MG staining, but lower MDR signal (referred as MDR/MG^{lo}) was increased in tumors compared to T cells from spleens and dLNs of tumor-bearing mice

(**Figure 2a** and **Extended Data Figure 2b**). By examining $CD8^+$ T cells in peripheral blood mononuclear cells (PBMCs) and tumor infiltrated lymph nodes (TILNs) from melanoma patients, we confirmed that $CD8^+$ TILs from the majority of patients contained more of the MDR/MG^{lo} population (**Figure 2b**). To further examine whether MDR/MG^{lo} cells can be seen in tumor-specific $CD8^+$ T cells, we transferred OT-I T cells (ovalbumin-specific TCR transgenic T cells) into mice engrafted with YUMM1.7 melanoma cells overexpressing ovalbumin (YUMM1.7-OVA) and found that a higher fraction of MDR/MG^{lo} OT-I TILs compared to splenic OT-I cells (**Extended Data Figure 2c**). To scrutinize the mitochondrial phenotypes in MDR/MG^{hi} and MDR/MG^{lo} populations, we examined mitochondrial ultrastructure of MDR/MG^{hi} and MDR/MG^{lo} TILs and found that mitochondria in MDR/MG^{lo} TILs were disrupted with fewer crista and decreased cristae length (**Figure 2c-e**). We further found that MDR/MG^{lo} TILs displayed higher MG signals, but contained less mtDNA and produced higher level of mtROS (**Figure 2f-h**), suggesting that the mitochondria accumulating in MDR/MG^{lo} TILs are depolarized and dysfunctional. To investigate whether mitochondria in MDR/MG^{lo} TILs are functionally impaired, we treated cells with oligomycin to inhibit electron transport chain (ETC) complex V, which can result in a lower increase in mitochondrial membrane potential when the respiratory chain of mitochondria is ceased[33]. Our results showed that the MDR/MG^{lo} population had a lower fold change in mitochondrial membrane potential upon oligomycin treatment (**Extended Data Figure 2d**), suggesting that MDR/MG^{lo} TILs contain depolarized mitochondria that exhibit reduced respiratory activity.

Since mitophagy is a critical cellular function for mitochondrial quality control and cells with impaired mitophagy activity have been shown to accumulate depolarized mitochondria[34], we then postulated that $CD8^+$ TILs may have impaired mitophagy activity that impinges on the clearance of damaged mitochondria. We generated an OT-I mouse strain stably expressing MitoQC reporter, which enables visualization of mitophagy with a tandem mCherry-GFP-tagged FIS1 reporter[35], to illuminate mitophagy *in vivo* by measuring GFP/mCherry fluorescence ratios. We found that OT-I TILs exhibited lower mitophagy activity compared to splenic OT-I cells (**Figure 2i-j**). Since mitophagy is a selective autophagy, we then examined whether autophagy was also compromised by exploiting an autophagy reporter system[36] and found OT-I TILs exhibited reduced autophagy events (**Figure 2k-l**). To confirm the contribution of a mitophagy defect to the development of the depolarization phenotype, we conditionally ablated the expression of *Park2*, a gene encoding Parkin for controlling mitophagy[34], in P14 cells (gp33-specific TCR transgenic T cells) (referred as $Park2^{cko}$) and examined mitochondrial phenotypes in transferred cells. Our result showed that *Park2*-deficient P14 TILs acquired mitochondrial depolarization faster and a more severe depolarization phenotype compared to wild-type P14 TILs (**Figure 2m**), suggesting that disruption of mitophagy machinery further enhances the mitochondrial depolarization phenotype in $CD8^+$ TILs.

CD8$^+$ TILs with depolarized mitochondria are terminally exhausted

Emerging evidence has revealed that T cells with mitochondrial abnormalities display impaired effector functions[13, 14, 37]. However, it remains unknown whether reduced mitochondrial fitness in CD8$^+$ TILs imprints permanent T cell dysfunction. We found that MDR/MG^{lo} TILs expressed higher levels of PD-1 and decreased T-bet expression (**Figure 3a-b**), suggesting that TILs accumulating depolarized mitochondria may lose effector function. Indeed, MDR/MG^{lo} TILs produce less interferon-γ (IFN-γ) and tumor necrosis factor (TNF) compared to the MDR/MG^{hi} population. Surprisingly, IL-2/IL-15 exposure boosted the production of IFN-γ and TNF in MDR/MG^{hi} TILs, but not in MDR/MG^{lo} TILs (**Figure 3c-d**). Since IL-15 treatment has been shown to restore effector function in partially exhausted, but not terminally exhausted, CD8$^+$ T cells[21, 38], our results suggest that MDR/MG^{lo} TILs might be terminally exhausted. By examining the transcriptomic differences, we found that MDR/MG^{hi} TILs had higher expression of genes associating with memory and effector T cells; however, MDR/MG^{lo} TILs up-regulated gene hits linking with IFN-γ signature and high PD-1 expression (**Figure 3e**). Gene-set-enrichment analysis (GSEA) confirmed that MDR/MG^{lo} TILs were enriched in gene signatures of exhausted CD8$^+$ T cells (**Figure 3f**). In support of down-regulated expression of TCF1-regulated genes in memory T cells[29, 39] in MDR/MG^{lo} TILs, we found that MDR/MG^{lo} TILs expressed lower levels of TCF1 compared to MDR/MG^{hi} population (**Figure 3g**). We next investigated whether MDR/MG^{lo} TILs display characteristics of terminally exhausted T cells by transferring splenic OT-I cells and MDR/MG^{hi} and MDR/MG^{lo} OT-I TILs isolated from melanoma-bearing mice into naïve C57BL/6 mice, followed by infection with *Listeria monocytogenes* expressing OVA peptide (*Lm*-OVA). In this setting, CD8$^+$ T cells committing to terminal exhaustion will undergo less population re-expansion and the expanded population will inherit exhausted features, including sustained expression of exhaustion markers and compromised production of effector cytokines, upon *Lm*-OVA infection[18, 19]. We found that MDR/MG^{lo} TILs underwent less population expansion compared to MDR/MG^{hi} TILs and splenic OT-I cells (**Figure 3h**). Moreover, OT-I cells re-expanded from MDR/MG^{lo} TILs expressed higher amounts of PD-1 and LAG-3, but produced less IFN-γ (**Figure 3i-k**), indicating that the exhaustion characteristics of MDR/MG^{lo} TILs are permanent. Taken together, our data reveal that accumulation of depolarized mitochondria in CD8$^+$ TILs propels T cells towards terminal exhaustion and locks them in a permanent dysfunctional state.

Depolarized mitochondria link with exhaustion epigenetic programs

Terminally exhausted CD8$^+$ T cells have been shown to exhibit distinct epigenetic landscapes, including chromatin accessibility and DNA methylation patterns, from effector CD8$^+$ T cells[6, 20, 21, 22]. Therefore, we

investigated whether TILs accumulating depolarized mitochondria display alterations of epigenetic landscapes. By examining chromatin accessibility with the Assay for Transposase-Accessible Chromatin sequencing (ATAC-seq), we identified that 709 genomic regions characterized by higher chromatin accessibility in MDR/MG^{hi} TILs, whereas 2564 regions had increased chromatin accessibility in MDR/MG^{lo} TILs (**Figure 4a**). The regions that were more accessible in MDR/MG^{hi} TILs were mostly located in the intronic regions and downstream of gene promoters, whereas most of the differentially accessible loci in MDR/MG^{lo} TILs were located in the upstream regions and 5' UTR, which contain most of the regulatory elements (**Figure 4b**). Interestingly, the differentially accessible peaks in MDR/MG^{lo} TILs were enriched in gene signatures of exhausted CD8^{+} T cells (**Figure 4c**), indicating that MDR/MG^{lo} TILs are more exhausted and less memory-like compared to MDR/MG^{hi} TILs. Ontology analyses of the impacted genomic loci more accessible in MDR/MG^{hi} TILs showed significant enrichment of cellular programs involved in PDGFR-β signaling and β-catenin-mediated signaling, but MDR/MG^{lo} TILs exhibited more accessible gene loci coupled to the SMAD2/3 signaling, IFN-γ pathway and p53 signaling pathway, which has been reported to be associated with T cell exhaustion in HCV-specific T cells [40] (**Figure 4d-e**). We next found that the regions more accessible in MDR/MG^{lo} TILs showed enrichment in the consensus binding motifs of YY1 and ER-stress-responding TF motifs, which have been shown to participate T cell exhaustion[41, 42] (**Figure 4f**). Intriguingly, binding motifs for transcription factors involved in memory T cell-related functions, including Foxo1 and Runx, were enriched in the genomic regions differentially open in MDR/MG^{hi} TILs. We also observed that chromatin peaks in both *Tcf7* and *Lef1* locus were less accessible in MDR/MG^{lo} CD8^{+} TILs (**Figure 4g**), suggesting that the TILs accumulating depolarized mitochondria lost TCF1 expression and downstream signaling. Of note, a more accessible peak was observed in *Hif1a* locus in MDR/MG^{lo} TILs, suggesting that CD8^{+} TILs with depolarized mitochondria may endure hypoxic stress.

Furthermore, we performed whole genome bisulfite sequencing (WGBS) analysis and identified differentially methylated CpG dinucleotides in MDR/MG^{lo} TILs compared to MDR/MG^{hi} population, and vice versa. The distributions of differentially methylated CpG dinucleotides within gene loci were similar between these two populations; however, more robust differences can be seen in CpG island and promoter regions (**Extended Data Figure 3a-c**). Since methylations in CpG islands and promoter regions are tightly linked to the repressive regulation of transcription[22, 43], we focused on differentially methylated CpG islands and promoters for the following analyses. Ontology analyses of the impacted genes hypomethylated in the promoter regions of MDR/MG^{hi} TILs also showed significant enrichment in β-catenin-mediated signaling, but hypomethylated regions in MDR/MG^{lo} TILs were enriched in genes coupled to the p53 signaling pathway and DNA repairing signaling (**Extended Data Figure 3d-e**). Motif enrichment analysis revealed that the hypomethylated regions in MDR/MG^{hi} CD8^{+} TILs were enriched in

consensus binding motifs for transcription factors associated with T cell activation and memory T cell formation (**Extended Data Figure 3f**). Collectively, our findings reveal that MDR/MG^{lo} CD8^{+} TILs display epigenetic features, including chromatin accessibility and DNA methylation, that have been reported to associate with terminal exhaustion.

TCR and PD-1 signals drive accumulation of depolarized mitochondria

We observed that TILs from more advanced tumor stages had a higher percentage harboring depolarized mitochondria (**Figure 5a**), suggesting that mitochondrial activity in TILs decline in a tumor progression-dependent manner. Next, we engrafted YUMM1.7 melanoma cells overexpressing either ovalbumin (YUMM1.7-OVA) or glycoprotein 33 of lymphocytic choriomeningitis virus (YUMM1.7-gp33) in different flanks of wild type mice. Then, we adoptively transferred both OT-I and P14 CD8^{+} T cells into tumor-bearing mice to examine mitochondrial fitness of the transferred T cells, a setting allowing us to determine whether the ability to recognize tumor antigens contributes to mitochondrial dysfunction in CD8^{+} TILs. Our results showed that more OT-I cells infiltrating YUMM1.7-OVA tumors contained depolarized mitochondria compared to P14 cells in the same tumors. In contrast, a higher fraction of P14 cells displayed mitochondrial dysfunction in YUMM1.7-gp33 tumors (**Figure 5b-c**); however, transferred cells in both spleen and dLNs displayed similar mitochondrial fitness (**Extended Data Figure 4a**). Together, these results suggest that TCR stimulation in the TME suppresses mitochondrial fitness in TILs. We then speculated that TCR affinity to antigen might stimulate the formation of TILs with a depolarized mitochondrial phenotype. We took advantage of OT-3 TCR transgenic mice, in which CD8^{+} T cells express TCR recognizing the OVA peptide-MHCI complex (pMHCI) with a 50-fold weaker affinity as compared to OT-I cells[44]. We co-transferred OT-I and OT-3 T cells into YUMM1.7-OVA tumor-bearing mice and then examined their mitochondrial fitness. A higher percentage of OT-I TILs harbored depolarized mitochondria compared to OT-3 TILs in the same tumor (**Figure 5d**), but OT-I and OT-3 cells in spleens and dLNs displayed comparable mitochondrial fitness (**Extended Data Figure 4b**), indicating that a higher affinity of TCR:pMHCI interaction facilitates mitochondrial dysfunction in TILs. We also found that human TILs with a depolarized mitochondrial phenotype had higher clonality of the TCR beta chain (**Figure 5e**). Since human TILs displaying a more restricted TCR repertoire (high TCR clonality), which implies a better ability to recognize tumor antigens, exhibited more severe exhaustion[45], these results suggested that TILs with better ability to recognize tumor antigens tend to accumulate depolarized mitochondria, supporting commitment to T cell exhaustion. We next examined whether PD-1 expression, a co-inhibitory receptor that has been shown to support T exhaustion and metabolic insufficiency[12, 46], could stimulate formation of TILs with depolarized mitochondria. We co-transferred wild-type and PD-1-deficient (PD-1 KO) OT-I cells into YUMM1.7-OVA tumor-bearing mice. We found

that PD-1 KO TILs contained a smaller population with depolarized mitochondria accumulation (**Figure 5f**) even though PD-1 KO and wild-type cells in spleens and dLNs had similar mitochondrial fitness (**Extended Data Figure 4c**). Taken together, our results identify factors suggested to drive T cell exhaustion, including affinity of TCR:pMHCI interaction and PD-1 signaling, that can abrogate mitochondrial fitness in TILs.

Metabolic stress coordinates with TCR signal to impair mitochondrial fitness

We found that MDR/MG^{lo} TILs expressed lower amounts of hypoxia-suppressed genes (**Extended Data Figure 5a**), suggested that MDR/MG^{lo} CD8^{+} TILs might be under hypoxic stress. Moreover, by computationally weighting the metabolic programs of individual human CD8^{+} TILs[47], we observed that terminally exhausted TILs expressed higher levels of hypoxia gene signatures (**Extended Data Figure 5b-c**). We reasoned that the coordination of TCR stimulation, hypoxia and tumor-derived factors could induce a dysfunctional mitochondrial phenotype in CD8^{+} TILs. We found that stimulating Mito-QC CD8^{+} T cells with TCR stimulus and hypoxia, but not tumor cell-conditioned medium (TCM), suppressed mitophagy (**Figure 6a** and **Extended Data Figure 5d**). We next found that TCR stimulation coordinated with hypoxia and TCM to maximize the formation of MDR/MG^{lo} T cells in a time-dependent manner (**Figure 6b** and **Extended Data Figure 5e-f**). Moreover, the MDR/MG^{lo} population generated in this *in vitro* culture displayed disorganized crista morphology (**Figure 6c-e**). To determine whether *in vitro*-generated MDR/MG^{lo} CD8^{+} T cells display terminally exhausted features, we adoptively transferred *in vitro*-generated MDR/MG^{hi} and MDR/MG^{lo} OT-I cells into naïve mice followed by *Lm*-OVA rechallenge. Our result showed that the *in vitro*-generated MDR/MG^{lo} CD8^{+} T cells displayed reduced proliferative capacity, elevated expression of PD-1 and LAG-3, and reduced production of effector cytokines compared to MDR/MG^{hi} CD8^{+} T cells (**Figure 6f-h**), indicating that our *in vitro* culture mimics the tumor microenvironmental stress that is needed for disrupting mitochondrial fitness and reinforcing the exhaustion program in T cells.

Hypoxia induces aerobic glycolysis to fulfill metabolic demands as a metabolic adaptation; however, cells simultaneously experiencing both hypoxia and glucose deprivation elicit mitochondrial dysfunction in a mtROS-dependent manner[48]. We then speculated that scavenging mtROS might prevent formation of MDR/MG^{lo} T cells. Indeed, supplementation with a mitochondria-targeted antioxidant, MitoTempo, effectively ameliorated formation of MDR/MG^{lo} T cells (**Extended Data Figure 5g**). Furthermore, we found that treatment with mitochondrial uncouplers to induce mitochondrial damage plus TCR stimulation drastically boosted accumulation of depolarized mitochondria, but mitochondrial uncouplers alone failed to affect mitochondrial fitness in CD8^{+} T cells (**Extended Data Figure 5h**), suggesting that accumulation of depolarized mitochondria in T cells might result from the cooperation of

mitophagy impairment and mitochondrial damage. In support of this notion, treatment with oligomycin plus Mdivi-1, an inhibitor that interrupts the initiation of mitophagy, stimulated formation of MDR/MG^{lo} population in both murine (**Figure 6i**) and human CD8^{+} T cells (**Extended Data Figure 5i**). Of note, we also found that glucose supplementation reduced accumulation of depolarized mitochondria in both murine and human CD8^{+} T cells in the *in vitro* culture system (**Figure 6j** and **Extended Data Figure 5j**), suggesting that preventing inappropriate metabolic reprogramming induced by oxygen and glucose deprivation sustain mitochondrial fitness in TILs. Collectively, our data strongly demonstrate how TCR stimulation coordinates with hypoxia and tumor cell-conditioned medium to impair mitochondrial fitness in T cells.

Dysfunctional mitochondria dictate exhaustion in CD8^{+} T cells

To determine whether disturbed mitochondrial fitness instructs commitment to T cell exhaustion, MDR/MG^{hi} and MDR/MG^{lo} OT-I cells generated by treatment with oligomycin plus Mdivi-1 for 6 h without introducing TCR signaling and tumor derived were transferred into naïve mice which were subsequently infected with *Lm*-OVA**.** We found that *in vitro* generated MDR/MG^{lo} OT-I cells displayed reduced proliferative capacity, elevated expression of PD-1 and LAG-3, and reduced production of effector cytokines compared to MDR/MG^{hi} OT-I cells (**Figure 7a-d**), implying that forced accumulation of depolarized mitochondria is sufficient to reinforce a fixed exhaustion program in CD8^{+} T cells. We further found that the differentially accessible genomic loci in the *in vitro* generated MDR/MG^{lo} T cells were mainly located in the upstream regions and 5' UTR (**Extended Data Figure 6a**). GSEA of the differentially accessible loci in MDR/MG^{lo} and MDR/MG^{hi} CD8^{+} T cells generated from the *in vitro* culture also exhibited strong enrichments with the accessible loci derived from the comparison between MDR/MG^{lo} and MDR/MG^{hi} CD8^{+} TILs (**Figure 7e**), indicating a high similarity between *in vivo* and *in vitro* ATAC-seq results. We also found that memory-related TF binding motifs were enriched in differentially accessible regions in MDR/MG^{hi} CD8^{+} T cells, whereas binding motifs for transcription factors involved in ER-stress were enriched in MDR/MG^{lo} CD8^{+} T cells (**Figure 7f**). BioCarta pathway analyses also revealed that p53 pathway were enriched in genes with differentially accessible peaks between MDR/MG^{hi} and MDR/MG^{lo} CD8^{+} T cells generated from the *in vitro* culture (**Extended Data Figure 6b**). Importantly, both *Tcf7* and *Lef1* loci were also less accessible in the *in vitro* generated MDR/MG^{lo} CD8^{+} T cells (**Extended Data Figure 6c**). Overall, these results provide evidence that interrupting the mitochondrial fitness of CD8^{+} T cells is sufficient to orchestrate epigenetic reprogramming associated with exhaustion establishment.

Nicotinamide ribose prevents declined mitochondrial fitness

Given that nicotinamide adenine dinucleotide (NAD) has been reported to stimulate mitophagy and in a variety of cells, we speculated that supplementation precursors for generating NAD could prevent $CD8^+$ T cells from undergoing exhaustion and stimulate anti-tumor immunity[49]. We found that the NAD level in $CD8^+$ T cells was elevated upon treatment with nicotinamide (NAM) and nicotinamide riboside (NR), but not nicotinic acid (NA) (**Extended Data Figure 7a**). We further found that NR significantly reduced the accumulation of depolarized mitochondria in a Drp-1-dependent manner and attenuated mtROS levels in $CD8^+$ T cells (**Figure 8a-c**), suggesting that mitophagy is required for NR-induced protection of mitochondrial fitness in $CD8^+$ T cells. Next, we examined whether NR could enhance the anti-tumor responses of T cells within the TME. Strikingly, administration of alginate-mixed NR via intratumoral injection induced robust suppression of melanoma growth, reduced the abundance of MDR/MG^{lo} TILs accompanying with attenuated mtROS level, and boosted OT-I $CD8^+$ TILs to produce effector cytokines (**Figure 8d-g**), indicating that NR can sustain mitochondrial fitness and anti-tumor effector functions in TILs. We next investigated whether oral treatment with NR could elicit anti-tumor responses and found that $CD8^+$ and $CD4^+$ T cells were increased in NR-fed mice compared to chow diet control (**Extended Data Figure 7b**). Moreover, melanoma and colon tumor growth was significantly impeded in NR-fed mice and combined treatment with the NR diet and immune checkpoint blockade elicited additive anti-tumor responses (**Figure 8h** and **Extended Data Figure 7c**). Importantly, NR treatment failed to suppress tumor growth when we depleted $CD8^+$ T cells in melanoma-bearing mice (**Figure 8i**), suggesting that NR treatment induced anti-tumor responses in a $CD8^+$ T cell-dependent manner. Collectively, these findings reveal that supplementation with NR alleviates mitochondrial dysfunction and further induces additive anti-tumor immunity in conjunction with ICB treatments.

Discussion

Here, we show that sustained metabolic restrictions plus TCR stimulation drive accumulation of depolarized mitochondria in $CD8^+$ TILs. We further reveal that forcing depolarized mitochondria accumulation by disturbing mitochondrial dynamics reinforces phenotypic and epigenetic reprogramming for T cell exhaustion. Lastly, treatment with nicotinamide riboside presents as a promising strategy to prevent mitochondrial dysfunction and improve responsiveness to PD-1 blockade treatment. Together, these results provide new insights into how distorted mitochondrial activity is induced in $CD8^+$ TILs to drive the regulatory circuit toward terminally exhausted T cells.

In response to glucose deprivation, cells engage mitochondrial fusion to boost oxidative phosphorylation (OXPHOS)[5]. However, hypoxia stimulates aerobic glycolysis to support metabolic demands. Cells simultaneously encountering these metabolic challenges force robust production of mtROS in response to the metabolic chaos caused by the opposing metabolic programs[48]. Since $CD8^+$

TILs contain depolarized and physically close mitochondria, it is likely that $CD8^+$ TILs initially increase mitochondrial dynamics and activity to combat glucose deprivation in the TME. As a trade-off of this action, mtROS may further damage mitochondria. This is supported by our results that supplementation with glucose and mitochondria-targeted antioxidant, MitoTempo, ameliorates formation of MDR/MG^{lo} population. We also observe that PD-1 signaling supports accumulation of depolarized mitochondria in $CD8^+$ TILs. Since PD-1 signaling can suppress glycolytic activity but stimulate OXPHOS[46], it is possible the engagement of PD-1 signaling may elevate mtROS production and mitochondrial damage in the hypoxic microenvironment by suppressing glucose utilization. Moreover, our results show that TCR-driven mitophagy impairment contributes to mitochondrial dysfunction. Interestingly, TCR stimulation activates mammalian target of rapamycin (mTOR), and elevated mTOR activity is known to suppress autophagy and mitophagy activity. Of note, $CD8^+$ TILs and exhausted T cells generated from chronic lymphocytic chroiomeningitis (LCMV) infection have been reported to display sustained mTOR activation[12, 14, 50], and inhibiting mTOR during chronic LCMV infection reduced accumulation of depolarized mitochondria in early activated virus-specific $CD8^+$ T cells[12]. Therefore, it will be of interest to elucidate whether persistent TCR stimulation in $CD8^+$ TILs impedes mitophagy in an mTOR-dependent manner in future studies.

Accumulation of depolarized mitochondria is known to induce senescence, an altered secretome, and metabolic vulnerability in aged cells by modulating nuclear events, including DNA replication, transcription and damage responses, through retrograde signals generated from mitochondria[9]. Emerging evidence indicates that epigenetic alterations might be the major regulatory mechanism to link mitochondrial activity with nuclear reprogramming. Since our results imply that accumulation of depolarized mitochondria in $CD8^+$ T cells is sufficient to induce epigenetic reprogramming, we speculate that altered retrograde signals caused by a decline in mitochondrial fitness might play a determinative role in epigenetic reprogramming. Thus, identifying the metabolic differences and the underlying retrograde signals responsible for epigenetic reprogramming would provide critical information for sustaining and even re-reprogramming the epigenetic landscape to support productive T cell anti-tumor responses.

Acknowledgments

We thank W.-L. Lo, S.C.-C. Huang and L.-F. Lu for insightful comments. We thank A. Nemc for preparing the WGBS libraries, V. Gernedl for preparing the ATAC-seq libraries and the Biomedical Sequencing Facility at CeMM for assistance with next generation sequencing. We also thank M. Bosenberg (Yale University) for providing YUMM1.7 melanoma cells, T. Dawson (Johns Hopkins School of Medicine) for providing *Park2*$^{flox/flox}$ mice, I. Ganley (University of Dundee) for providing Mito-QC mice and R. Ahmed (Emory University) for providing autophagy reporter. We thank the instrumental

supports from the EM facility of the biomedical sciences and the ASCEM in Academia Sinica. P.-C.H. was supported in part by the SNSF project grants (31003A_163204 and 31003A_182470), the Swiss Institute for Experimental Cancer Research (ISREC 26075483) and European Research Council Staring Grant (802773-MitoGuide). N.V. was supported by the Kristian Gerhard Jebsen Foundation. Austrian Science Fund (FWF) Special Research Programme grant, New Frontiers Group award of the Austrian Academy of Sciences and ERC Starting Grant (679146) to C.B. P.-S.L. was supported by the Ministry of Science and Technology grant (MOST-108-2320-B-400-025-MY3) and National Health Research Institute grant (NHRI-CS-108-PP-09). L.T. was supported in part by Swiss National Science Foundation (Project grant 315230_173243) and Swiss Cancer League (No. KFS-4600-08-2018). A.Z. was supported by Cancer League Switzerland (KFS-3394-02-2014) and SNSF project grant (320030_162575). C.J. was supported by the Swiss Cancer League (KFS-3710-08-2015), SNSF grant (PROOP3_179727) and the Ludwig Institute for Cancer Research.

Author Contributions

Y.-R.Y., N.V. and P.-C.H. designed the research. Y.-R.Y., H.W., T.C., W.-C.C., and M.R.R. performed in vitro and in vivo experiments. H.I. and C.B. conducted epigenome analyses and Z.X. and J.W.L. performed computational analysis of single-cell RNA-sequencing. F.F., Y.-F.J. and P.-S.L. performed electron microscopy analyses and confocal microscope analysis. M.G. and L.T. supported the production of NR-loaded alginate hydrogel. C.J. and A.Z. provided human samples. R.G. and G.C. performed human TIL TCR sequencing and analysis. Y.-R.Y., H.W., H.I. and N.V. analyzed the results. Y.-R.Y. and P.-C.H. wrote the manuscript.

Competing Interests Statement

P.-C.H. is serving as a member of scientific advisory board for Elixiron Immunotherapeutics and Acepodia and receiving research grants from Elixiron Immunotherapeutics, Roche and Novartis. P.-C.H. received honorarium from Pfizer and Chugai.

References

1. Li, X. *et al.* Navigating metabolic pathways to enhance antitumour immunity and immunotherapy. *Nat Rev Clin Oncol* **16**, 425-441 (2019).

2. Hanahan, D. & Coussens, L.M. Accessories to the crime: functions of cells recruited to the tumor microenvironment. *Cancer Cell* **21**, 309-322 (2012).

3. Ho, P.C. *et al.* Phosphoenolpyruvate Is a Metabolic Checkpoint of Anti-tumor T Cell Responses. *Cell* **162**, 1217-1228 (2015).

4. Chang, C.H. *et al.* Metabolic Competition in the Tumor Microenvironment Is a Driver of Cancer Progression. *Cell* **162**, 1229-1241 (2015).

5. Rambold, A.S., Kostelecky, B., Elia, N. & Lippincott-Schwartz, J. Tubular network formation protects mitochondria from autophagosomal degradation during nutrient starvation. *Proc Natl Acad Sci U S A* **108**, 10190-10195 (2011).

6. Pauken, K.E. *et al.* Epigenetic stability of exhausted T cells limits durability of reinvigoration by PD-1 blockade. *Science* **354**, 1160-1165 (2016).

7. Sun, N., Youle, R.J. & Finkel, T. The Mitochondrial Basis of Aging. *Mol Cell* **61**, 654-666 (2016).

8. Wiley, C.D. *et al.* Mitochondrial Dysfunction Induces Senescence with a Distinct Secretory Phenotype. *Cell Metab* **23**, 303-314 (2016).

9. Quiros, P.M., Mottis, A. & Auwerx, J. Mitonuclear communication in homeostasis and stress. *Nat Rev Mol Cell Biol* **17**, 213-226 (2016).

10. van der Windt, G.J.W. *et al.* Mitochondrial Respiratory Capacity Is a Critical Regulator of CD8(+) T Cell Memory Development. *Immunity* **36**, 68-78 (2012).

11. Buck, M.D. *et al.* Mitochondrial Dynamics Controls T Cell Fate through Metabolic Programming. *Cell* **166**, 63-76 (2016).

12. Bengsch, B. *et al.* Bioenergetic Insufficiencies Due to Metabolic Alterations Regulated by the Inhibitory Receptor PD-1 Are an Early Driver of CD8(+) T Cell Exhaustion. *Immunity* **45**, 358-373 (2016).

13. Scharping, N.E. *et al.* The Tumor Microenvironment Represses T Cell Mitochondrial Biogenesis to Drive Intratumoral T Cell Metabolic Insufficiency and Dysfunction. *Immunity* **45**, 374-388 (2016).

14. Siska, P.J. *et al.* Mitochondrial dysregulation and glycolytic insufficiency functionally impair CD8 T cells infiltrating human renal cell carcinoma. *JCI Insight* **2**(12):e93411 (2017).

15. Baitsch, L. *et al.* Exhaustion of tumor-specific CD8(+) T cells in metastases from melanoma patients. *J Clin Invest* **121**, 2350-2360 (2011).

16. Wherry, E.J. & Kurachi, M. Molecular and cellular insights into T cell exhaustion. *Nat Rev Immunol* **15**, 486-499 (2015).

17. Alfei, F. & Zehn, D. T Cell Exhaustion: An Epigenetically Imprinted Phenotypic and Functional Makeover. *Trends Mol Med* **23**, 769-771 (2017).

18. Utzschneider, D.T. *et al.* T cells maintain an exhausted phenotype after antigen withdrawal and population reexpansion. *Nat Immunol* **14**, 603-610 (2013).

19. Schietinger, A. *et al.* Tumor-Specific T Cell Dysfunction Is a Dynamic Antigen-Driven Differentiation Program Initiated Early during Tumorigenesis. *Immunity* **45**, 389-401 (2016).

20. Sen, D.R. *et al.* The epigenetic landscape of T cell exhaustion. *Science* **354**, 1165-1169 (2016).

21. Philip, M. *et al.* Chromatin states define tumour-specific T cell dysfunction and reprogramming. *Nature* **545**, 452-456 (2017).

22. Ghoneim, H.E. *et al.* De Novo Epigenetic Programs Inhibit PD-1 Blockade-Mediated T Cell Rejuvenation. *Cell* **170**, 142-157 e119 (2017).

23. Mognol, G.P. *et al.* Exhaustion-associated regulatory regions in CD8(+) tumor-infiltrating T cells. *Proc Natl Acad Sci U S A* **114**, E2776-E2785 (2017).

24. Chen, Z. *et al.* TCF-1-Centered Transcriptional Network Drives an Effector versus Exhausted CD8 T Cell-Fate Decision. *Immunity* **51**, 840-855 (2019).

25. Jadhav, R.R. *et al.* Epigenetic signature of PD-1+ TCF1+ CD8 T cells that act as resource cells during chronic viral infection and respond to PD-1 blockade. *Proc Natl Acad Sci U S A* **116**, 14113-14118 (2019).

26. Im, S.J. *et al.* Defining CD8+ T cells that provide the proliferative burst after PD-1 therapy. *Nature* **537**, 417-421 (2016).

27. Utzschneider, D.T. *et al.* T Cell Factor 1-Expressing Memory-like CD8(+) T Cells Sustain the Immune Response to Chronic Viral Infections. *Immunity* **45**, 415-427 (2016).

28. Siddiqui, I. *et al.* Intratumoral Tcf1(+)PD-1(+)CD8(+) T Cells with Stem-like Properties Promote Tumor Control in Response to Vaccination and Checkpoint Blockade Immunotherapy. *Immunity* **50**, 195-211 e110 (2019).

29. Miller, B.C. *et al.* Subsets of exhausted CD8(+) T cells differentially mediate tumor control and respond to checkpoint blockade. *Nat Immunol* **20**, 326-336 (2019).

30. Dankort, D. *et al.* Braf(V600E) cooperates with Pten loss to induce metastatic melanoma. *Nat Genet* **41**, 544-552 (2009).

31. Pendergrass, W., Wolf, N. & Poot, M. Efficacy of MitoTracker Green and CMXrosamine to measure changes in mitochondrial membrane potentials in living cells and tissues. *Cytometry A* **61**, 162-169 (2004).

32. Palikaras, K., Lionaki, E. & Tavernarakis, N. Mechanisms of mitophagy in cellular homeostasis, physiology and pathology. *Nat Cell Biol* **20**, 1013-1022 (2018).

33. Zorova, L.D. *et al.* Mitochondrial membrane potential. *Anal Biochem* **552**, 50-59 (2018).

34. Narendra, D., Tanaka, A., Suen, D.F. & Youle, R.J. Parkin is recruited selectively to impaired mitochondria and promotes their autophagy. *J Cell Biol* **183**, 795-803 (2008).

35. McWilliams, T.G. *et al.* mito-QC illuminates mitophagy and mitochondrial architecture in vivo. *J Cell Biol* **214**, 333-345 (2016).

36. Xu, X. *et al.* Autophagy is essential for effector CD8(+) T cell survival and memory formation. *Nat Immunol* **15**, 1152-1161 (2014).

37. Song, M. *et al.* IRE1alpha-XBP1 controls T cell function in ovarian cancer by regulating mitochondrial activity. *Nature* **562**, 423-428 (2018).

38. Teague, R.M. *et al.* Interleukin-15 rescues tolerant CD8+ T cells for use in adoptive immunotherapy of established tumors. *Nat Med* **12**, 335-341 (2006).

39. Gattinoni, L. *et al.* Wnt signaling arrests effector T cell differentiation and generates CD8+ memory stem cells. *Nat Med* **15**, 808-813 (2009).

40. Barili, V. *et al.* Targeting p53 and histone methyltransferases restores exhausted CD8+ T cells in HCV infection. *Nat Commun* **11**, 604 (2020).

41. Balkhi, M.Y., Wittmann, G., Xiong, F. & Junghans, R.P. YY1 Upregulates Checkpoint Receptors and Downregulates Type I Cytokines in Exhausted, Chronically Stimulated Human T Cells. *iScience* **2**, 105-122 (2018).

42. Cao, Y. *et al.* ER stress-induced mediator C/EBP homologous protein thwarts effector T cell activity in tumors through T-bet repression. *Nat Commun* **10**, 1280 (2019).

43. Deaton, A.M. & Bird, A. CpG islands and the regulation of transcription. *Genes Dev* **25**, 1010-1022 (2011).

44. Enouz, S., Carrie, L., Merkler, D., Bevan, M.J. & Zehn, D. Autoreactive T cells bypass negative selection and respond to self-antigen stimulation during infection. *J Exp Med* **209**, 1769-1779 (2012).

45. Li, H. *et al.* Dysfunctional CD8 T Cells Form a Proliferative, Dynamically Regulated Compartment within Human Melanoma. *Cell* **176**, 775-789 e718 (2019).

46. Patsoukis, N. *et al.* PD-1 alters T-cell metabolic reprogramming by inhibiting glycolysis and promoting lipolysis and fatty acid oxidation. *Nat Commun* **6**, 6692 (2015).

47. Xiao, Z., Dai, Z. & Locasale, J.W. Metabolic landscape of the tumor microenvironment at single cell resolution. *Nat Commun* **10**, 3763 (2019).

48. Larsen, G.A., Skjellegrind, H.K., Berg-Johnsen, J., Moe, M.C. & Vinje, M.L. Depolarization of mitochondria in isolated CA1 neurons during hypoxia, glucose deprivation and glutamate excitotoxicity. *Brain Res* **1077**, 153-160 (2006).

49. Jang, S.Y., Kang, H.T. & Hwang, E.S. Nicotinamide-induced mitophagy: event mediated by high NAD+/NADH ratio and SIRT1 protein activation. *J Biol Chem* **287**, 19304-19314 (2012).

50. Staron, M.M. *et al.* The transcription factor FoxO1 sustains expression of the inhibitory receptor PD-1 and survival of antiviral CD8(+) T cells during chronic infection. *Immunity* **41**, 802-814 (2014).

Figure Legends

Figure 1. Tumor-infiltrating $CD8^+$ T cells display depolarized mitochondria

a, Mitochondrial mass and membrane potential of $CD8^+$ T cells isolated from indicated tissues of YUMM1.7 melanoma-bearing mice were examined by MitoTracker Green (MG) and MitoTracker Deep Red (MDR), respectively. **b**, **c**, Relative fold changes of mitochondrial mass, membrane potential (**b**) and the ratio of MDR to MG (**c**) in $CD8^+$ T cells isolated from indicated tissues (**b**, Spleen and Tumor: n = 20, dLN: n = 19; **c**, Spleen and Tumor: n = 24, dLN: n = 23). Fold changes were calculated by normalizing to the average intensity of indicated molecular probe in splenic T cells. **d**, **e**, Representative electron microscope images (**d**) and quantitative plots of mitochondrion number (**e**) in activated splenic and tumor-infiltrating $CD8^+$ T cells from tumor-bearing mice (n = 20 per group). Scale bars = 500 nm. **f**, The relative copy number of mitochondrial DNA (mtDNA) in activated splenic and tumor-infiltrating $CD8^+$ T cells from tumor-bearing mice (**f**, n = 6 per group). Fold changes were calculated by normalizing to the average copy number in splenic T cells. **g-i**, Representative electron microscope images (**g**) and quantitative plots of crista number (**h**) and length (**i**) per mitochondrion in activated splenic and tumor-infiltrating $CD8^+$ T cells from tumor-bearing mice (**h**, n = 50 per group; **i**, n = 50 per group). Scale bars = 500 nm. **j-m**, Representative 3D-electron microscope images (**j**) and quantitative plots of crista volume (**k**), normalized crista volume (**l**) and mitochondria-associated membrane (**m**) in activated splenic and tumor-infiltrating $CD8^+$ T cells. Each color in 3D images indicates one mitochondrion. (Spleen: n = 26; Tumor: n = 16). **n**, **o**, Mitochondrial ROS (**n**) and cytoplasmic ROS (**o**) in activated splenic and tumor-infiltrating $CD8^+$ T cells were determined by MitoSOX and CM-H2DCFDA staining, respectively (**n**, n = 11 per group; **o**, n = 6 per group). All data are mean ± s.e.m. and were analyzed by two-tailed, unpaired Student's *t*-test. Data are cumulative results from at least three independent experiments. Each symbol represents one individual (**b**, **c** and **f**).

Figure 2. Impaired mitophagy results in accumulation of depolarized mitochondria in $CD8^+$ TILs

a, Based on the ratio of MDR to MG, two distinct populations of $CD8^+$ TILs were determined as MDR/MG^{hi} (red) and MDR/MG^{lo} (blue) using flow cytometry (left panel), followed by the quantification of the percentage of MDR/MG^{lo} populations in activated $CD8^+$ T cells from spleens, dLNs and tumors of YUMM1.7 melanoma-engrafted mice (Spleen and Tumor: n = 20, dLN: n = 19). **b**, MDR/MG^{lo} populations were determined in human melanoma patients using flow cytometry (n = 11 per group). **c-e**, Representative electron microscope images (**c**) and quantitative results of crista length (**d**) and number (**e**) per mitochondrion in sorted MDR/MG^{hi} and MDR/MG^{lo} $CD8^+$ TILs (red arrowhead indicate crista) (MDR/MG^{hi}: n = 19; MDR/MG^{lo}: n = 18). Scale bar = 500 nm. **f**, The mitochondrial morphology of MDR/MG^{hi} and MDR/MG^{lo} $CD8^+$ TILs was detected by fluorescence confocal microscopy based on MG

staining. Scale bar = 2.5 μm. **g**, Copy number of mitochondrial DNA (mtDNA) of MDR/MG^{hi} and MDR/MG^{lo} CD8^{+} TILs was measured by PCR amplification (n = 6 per group). Fold changes were calculated by normalizing to the average copy number in splenic CD8^{+} T cells. **h**, Mitochondrial ROS was measured by MitoSOX staining in MDR/MG^{hi} and MDR/MG^{lo} CD8^{+} TILs (n = 11 per group). Results were normalized to the average mean fluorescence intensity of MitoSOX in MDR/MG^{hi} TILs. **i**, **j**, Mitophagy events in OT-I cells in the indicated tissues were detected by using MitoQC reporter system in which the lower gating areas of representative flow plots represent cells undergoing mitophagy (**i**) and the quantification of OT-I cells in indicated tissues engaging mitophagy (**j**) (n = 11 per group). **k**, **l**, Autophagy events were measured according to the lower gating area of representative flow plots (**k**), followed by the quantification of gated CD8^{+} T cells (**l**) (n = 9 per group). **m**, The representative flow plots (left) and the quantitative results of MDR/MG^{lo} populations in WT P14 and *Park2*^{cko} P14 CD8^{+} TILs (right) were determined by flow cytometry three days or eight days after transfer (n = 6 per group). All data are mean ± s.e.m. and were analyzed by two-tailed, unpaired Student's *t*-test. Data are cumulative results from at least three independent experiments. Each symbol or pair represents one individual (**a**, **b**, **g**, **h**, **j** and **l**).

Figure 3. CD8^{+} TILs accumulating depolarized mitochondria display characteristics of terminally exhausted T cells

a, **b**, Expression of PD-1 (**a**) and T-bet (**b**) in MDR/MG^{hi} and MDR/MG^{lo} CD8^{+} TILs was determined by flow cytometry (**a**, n= 13 per group; **b**, n = 6 per group). **c**, **d**, Production of TNF and IFN-γ in sorted MDR/MG^{hi} and MDR/MG^{lo} CD8^{+} TILs was measured by flow cytometry before and after *ex vivo* treatments of IL-15/IL-2 (**c**), followed by the quantifications of cytokine-producing cells as indicated (**d**) (MDR/MG^{hi}: *Ex vivo*, n = 16, IL-15/IL-2, n = 15; MDR/MG^{lo}: n = 5). **e**, Significantly enriched gene signatures from MSigDB in differential gene expression profile of MDR/MG^{hi} CD8^{+} TILs versus MDR/MG^{lo} CD8^{+} TILs from YUMM1.7-OVA tumors. **f**, GSEA of indicated signatures from the ranked list of genes differentially expressed in MDR/MG^{hi} CD8^{+} TILs versus MDR/MG^{lo} CD8^{+} TILs from YUMM1.7-OVA tumors. **g**, Expression of TCF1 in MDR/MG^{hi} and MDR/MG^{lo} CD8^{+} TILs was determined by flow cytometry (n = 6 per group). **h**, Total cellularity of expanded OT-I cells from indicated groups in spleens collected from *Lm*-OVA-re-challenged mice (Spleen and MDR/MG^{hi}, n = 16; MDR/MG^{lo}, n = 13). **i**, **j**, Expression of PD-1 (**i**) and LAG-3 (**j**) in expanded OT-I cells from indicated groups in spleens of *Lm*-OVA-re-challenged mice was determined by flow cytometry (**i**, Spleen: n = 16, MDR/MG^{hi}: n = 17, MDR/MG^{lo}: n = 14; **j**, Spleen: n = 8, MDR/MG^{hi}: n = 7, MDR/MG^{lo}: n = 10). **k**, The production of IFN-γ in expanded OT-I cells from indicated groups in spleens collected from *Lm*-OVA-re-challenged mice (Spleen and MDR/MG^{hi}: n = 16; MDR/MG^{lo}: n = 13). Floating boxes display the data

distribution from minimum to maximum with mean in the centre (**d** and **h**-**k**). All data were analyzed by two-tailed, unpaired Student's *t*-test. Data are cumulative results from at least three independent experiments. Each pair represents the comparison of TILs isolated from one tumor sample (**a**, **b** and **g**).

Figure 4. Mitochondrial fitness in TILs orchestrates epigenetic program

a, Heatmap with normalized chromatin accessibility exhibits cluster analysis of the 3273 differentially accessible peaks between MDR/MG^{hi} and MDR/MG^{lo} CD8^{+} TILs. **b**, Distributions of differentially accessible chromatin loci specific to MDR/MG^{hi} or MDR/MG^{lo} CD8^{+} TILs. **c**, GSEA of indicated signatures from the ranked list of differentially accessible peaks in MDR/MG^{hi} CD8^{+} TILs versus MDR/MG^{lo} CD8^{+} TILs from YUMM1.7-OVA tumors. **d**, **e**, Bar graphs represent NCI-Nature 2016 pathways that are significantly enriched among genes with accessible chromatin in MDR/MG^{hi} (**d**) and MDR/MG^{lo} (**e**) CD8^{+} TILs with indicated adjusted *P*-value. **f**, Significantly enriched transcription factor motifs in accessible genomic loci in MDR/MG^{hi} or MDR/MG^{lo} CD8^{+} TILs. Transcription factors labeled in green: involved in memory T cells formation or function; in purple: involved in ER-stress responses. NES, normalized enrichment score. **g**, Representative ATAC-seq tracks at *Tcf7*, *Lef1*, and *Hif1a* loci from sorted MDR/MG^{hi} or MDR/MG^{lo} CD8^{+} TILs. Differentially accessible regions are highlighted in blue. Scale bar = 10 kb.

Figure 5. TCR and PD-1 signals contribute to the accumulation of damaged mitochondria in TILs

a, MDR/MG^{hi} (red) and MDR/MG^{lo} (blue) populations were determined in CD8^{+} TILs isolated at the indicated day after tumor engraftment, followed by the quantification of the percentage of MDR/MG^{lo} population. (6d: n = 11; 12d: n = 12; 18d: n = 12; data are presented as mean ± s.e.m.) **b**, **c**, MDR/MG^{lo} populations in CD8^{+} OT-I and P14 TILs isolated from YUMM1.7-OVA and YUMM1.7-gp33 tumors were determined by flow cytometry (**b**) and further calculated in each mouse. Each line indicates paired TILs from same tumor (**c**, n = 13 per group). **d**, MDR/MG^{lo} populations in CD8^{+} OT-I and OT-3 TILs isolated from YUMM1.7-OVA tumors were determined using flow cytometry, and further quantified in each mouse. Each line indicates paired TILs from same tumor (n = 11 per group). **e**, Human TCR clonality was examined by RNAseq on TCRβ of MDR/MG^{hi} and MDR/MG^{lo} CD8^{+} TILs sorted from human colon cancer samples (left panel, representative flow plot), followed by the calculations of Simpson clonality index (right panel) (n = 4 per group). *P* values were assessed using the Wilconxon test. **f**, MDR/MG^{lo} populations in WT and PD-1 KO OT-I CD8^{+} TILs isolated from YUMM1.7-OVA tumors were determined using flow cytometry, followed by the quantifications of the percentage of MDR/MG^{lo} population (n = 12 per group). Data in **a**, **c**, **d**, and **f** were analyzed by two-tailed, unpaired Student's *t*-

test. Data are cumulative results from at least three independent experiments. Each symbol or pair represents one individual (**a** and **c**-**f**).

Figure 6. Coordination of TCR and metabolic stress drives mitochondrial dysfunction in CD8$^+$ T cells

a, **b**, Quantifications of mitophagy events (**a**) and MDR/MG^{lo} populations (**b**) of *in vitro*-activated CD8$^+$ OT1-Mito-QC and OT-I T cells, respectively, cultured under indicated conditions (**a**, n = 12 per group; **b**, n = 9 per group). TCM: tumor cell-conditioned medium; TCR: T cell receptor stimulation. **c**-**e**, Representative electron microscope images (**c**) and quantitative results of crista number (**d**) and length (**e**) in mitochondria of sorted MDR/MG^{hi} and MDR/MG^{lo} CD8$^+$ T cells generated under TCM/TCR/Hypoxia condition (red arrowhead indicate crista). Scale bar = 500 nm. (MDR/MG^{hi}: n = 64; MDR/MG^{lo}: n = 71) **f**, Total cellularity of expanded OT-I cells from indicated groups in spleens collected from *Lm*-OVA-re-challenged mice (n = 8 per group). **g**,**h**, Expression levels of PD-1 and LAG-3 (**g**), and the production of IFN-γ/TNF (**h**) in expanded OT-I cells from indicated groups in spleens collected from *Lm*-OVA-re-challenged mice (n = 8 per group). **i**, Quantitative results of MDR/MG^{lo} populations of *in vitro*-activated CD8$^+$ T cells treated with indicated compounds. (OA, oligomycin A) (n = 9 per group). **j**, Representative flow plots of MDR and MG stainings in *in vitro*-activated CD8$^+$ T cells cultured under TCM/TCR/Hypoxia condition supplemented with or without 10mM glucose (left) and the quantification of MDR/MG^{lo} populations in these conditions (right) (n = 9 per group). Floating boxes display the data distribution from minimum to maximum with mean in the centre (**f**-**h**). All data are mean ± s.d. and were analyzed by two-tailed, unpaired Student's *t*-test. Data are cumulative results from at least three independent experiments (**a**, **b**, **i** and **j**). Each symbol represents one individual (**f**-**h**).

Figure 7. Accumulation of depolarized mitochondria reinforces phenotypic and epigenetic exhaustion programs

a, Total cellularity of expanded OT-I cells from indicated groups in spleens collected from *Lm*-OVA-re-challenged mice (MDR/MG^{hi}: n = 14, MDR/MG^{lo}: n = 15). **b**-**d**, The expression level of surface exhaustion markers, PD-1 (**b**) and LAG-3 (**c**), and the production of IFN-γ/TNF (**d**) in expanded OT-I cells from indicated groups in spleens collected from *Lm*-OVA-re-challenged mice (**b**, **c**, MDR/MG^{hi}: n = 14, MDR/MG^{lo}: n = 15; **d**, n = 10 per group). **e**, GSEA of differentially accessible peaks in MDR/MG^{hi} and MDR/MG^{lo} CD8$^+$ T cells generated in vitro from the Log2FC ranked list of all the accessible peaks in MDR/MG^{hi} CD8$^+$ TILs versus MDR/MG^{lo} CD8$^+$ TILs from YUMM1.7-OVA tumors. **f**, Significantly enriched transcription factor motifs in peaks opening in MDR/MG^{hi} or MDR/MG^{lo} CD8$^+$ T cells generated from oligomycin and Mdivi-1 in vitro treatment. Transcription factors labeled in green:

involved in memory T cells formation or function; in purple: involved in ER-stress responses. Floating boxes display the data distribution from minimum to maximum with mean in the centre (**a**-**d**). All data were analyzed by two-tailed, unpaired Student's *t*-test. Each symbol represents one individual (**a**-**d**).

Figure 8. NR sustains mitochondrial fitness and anti-tumor responses in CD8$^+$ T cells

a, Representative flow plots of MDR and MG stainings in *in vitro*-activated CD8$^+$ T cells cultured under control condition or TCM/TCR/Hypoxia condition supplemented with or without 400μM NR (left) and the quantification of MDR/MG^{lo} populations in these conditions (right). TCM: tumor cell-conditioned medium; TCR: T cell receptor stimulation (n = 9 per group). **b**, Mitochondrial ROS in *in vitro*-activated CD8$^+$ T cells cultured under control condition or TCM/TCR/Hypoxia condition supplemented with or without 400μM NR was measured by MitoSOX staining (n = 3 per group). **c,** The quantification of MDR/MG^{lo} populations in control and Drp-1-deficient CD8$^+$ T cells cultured under control condition or TCR/TCM/Hypoxia condition supplemented with or without 400 μM NR (Ctrl gRNA: n = 6 per group; Drp1 gRNA: n = 9 per group). **d**, Tumor growth of YUMM1.7-OVA melanoma-engrafted mice received intratumoral injection with PBS or 400 μM NR in alginate (PBS-alginate: n = 8; NR-alginate: n = 7). **e**-**g**, *In vitro*-activated OT-I CD8$^+$ T cells were transferred into Yumm1.7-OVA melanoma-engrafted mice eight days post engraftment, followed by two injections of PBS- and NR-alginate into tumors on different flanks on day 8 and 11. CD8$^+$ TILs were isolated and analyzed on day 12. **e**, MDR/MG^{lo} populations in CD8$^+$ OT-I TILs isolated from PBS-treated and NR-treated YUMM1.7-OVA tumors were determined by flow cytometry and further calculated in each mouse. Each line indicates paired TILs from same mouse (n = 14 per group). **f**, The fold change of mitochondrial ROS between activated OT-I CD8$^+$ TILs isolated from PBS-treated and NR-treated YUMM1.7-OVA tumors (n = 19 per group). **g**, The fold change of TNF$^+$, IFN-γ$^+$ and TNF$^+$IFN-γ$^+$ cell populations in CD8$^+$ TILs isolated from PBS-treated and NR-treated YUMM1.7-OVA tumors (n = 15 per group). **h**, Tumor growth of YUMM1.7 melanoma-engrafted mice fed with indicated diet plus injection with PBS (Ctrl) or anti-PD-1 antibody (αPD-1). Red dotted lines indicate the tumor volume of 800 mm^3. **i**, Tumor growth of YUMM1.7 melanoma-engrafted mice fed with indicated diet and injected with either PBS or anti-CD8α antibody. Red dotted lines indicate the tumor volume of 800 mm^3. Data are mean ± s.d. and were analyzed by two-tailed, unpaired Student's *t*-test (**a**-**d**), whereas data were analyzed by two-tailed and paired Student's *t*-test in **e**-**g**. Data are cumulative results from at least three independent experiments. Each pair represents the comparison of TILs isolated from tumors with indicated treatments from one tumor-bearing mouse (**e**-**g**).

Methods

Mice

C57BL/6J, *Rag1*$^{-/-}$ (B6.129S7-Rag1tm1Mom/J), CD4-Cre (B6.Cg-Tg(Cd4-cre)1Cwi/BfluJ) and B6 Cas9 (B6J.129(Cg)-Gt(ROSA)26Sortm1.1(CAG-cas9-EGFP)Fezh/J) mice were purchased from Jackson Laboratory. *Pdcd1*$^{-/-}$ (PD-1 KO) mice were purchased from RIKEN. BrafCA;Tyr:CreER;*Pten*lox4-5 (Braf/Pten) mice were previously described [32]. Mito-QC mice [37] were provided by I.G. Ganley, and *Parkin*$^{fl/fl}$ mice [51] were provided by T.M. Dawson. Mito-QC mice were crossed with OT-I mice to obtain OT-I Mito-QC mice for adoptive cell transfer experiment. *Park2*^{cko} mice were generated by crossing *Parkin*$^{fl/fl}$ mice with P14 CD4-cre mice. All mice were housed in the animal facility of the University of Lausanne.

Tumor engraftment, treatments of tumor-bearing mice and re-challenge experiment

For tumor induction, 3-week-old Braf/Pten male mice were topically treated with 1 µl 4-hydroxytamoxifen (8 mg µl^{-1} in ethanol) on the skin surface. For tumor engraftment, tumor cell lines were injected (Yumm1.7: 5 × 10^4; Yumm1.7-OVA/gp33: 1× 10^6 cells; MC38: 2.5× 10^5 cells) subcutaneously into B6 or *Rag1*$^{-/-}$ mice, followed by the analysis on day 18. For the NR diet experiment, mice were fed with control chow diet or NR diet (400 mg kg^{-1}) starting on day 3 after tumor engraftment. The anti-PD-1 antibody (200 µg per injection, intraperitoneally, every 3 days, BioXcell, clone 29F.1A12) was injected intraperitoneally from day 7 post tumor engraftment, whereas the anti-CTLA4 (100 µg per injection, intraperitoneally, every 3 days, BioXcell, clone 9D9) was injected intraperitoneally from day 9 in MC38 tumor model. For the CD8-depletion experiment, mice were treated with anti-CD8 antibody (300 µg per injection, clone 2.43) every 3 days from day 3 post tumor engraftment. For the *Park2*^{cko} experiment, in vitro-activated *Park2*^{cko} CD8$^+$ T cells were adoptively transferred into Yumm1.7-gp33 melanoma-bearing mice on day 10 post tumor engraftment. For the CRISPR/Cas9-mediated Drp1-depletion experiment, *in vitro*-activated P14 Cas9 CD8$^+$ T cells were transduced with gRNAs, followed by adoptive transfer into Yumm1.7-gp33 melanoma-bearing mice on day 10 post-tumor engraftment. For NR intratumoral treatment, aqueous solution of NR (5 mg ml^{-1}, 41 µl, DI water) was mixed with an alginate solution (10 mg ml^{-1}, 2 ml, PBS), followed by the intratumoral injection to form hydrogel *in situ* within the tumor [52, 53, 54]. For *in vivo* re-challenge experiment, sorted MDR/MG^{hi} and MDR/MG^{lo} CD8$^+$ T cells from indicated conditions were transferred into naïve recipient mice, followed by the *Listeria monocytogenes* expressing OVA peptide (*Lm*-OVA) administration (5000 CFU per mouse), and analyzed the transferred cells 8 days

later. All experiments were conducted according to Swiss federal regulations and approved by the veterinary authority of Canton Vaud.

Cell lines and *in vitro* culture

The YUMM1.7 melanoma cell line was provided by M. Bosenberg as described previously [55, 56]. The YUMM1.7-OVA and YUMM1.7-gp33 cell lines were established by stably transduced parental cell lines with lentivirus harboring the expression cassettes of OVA or gp33 peptides and were maintained in high-glucose-supplemented Dulbecco's modified Eagle's medium (DMEM, Life Technologies) with 10% fetal bovine serum (Gibco), 100 U ml^{-1} penicillin-streptomycin (Thermo Fisher Scientific) and puromycin (InvivoGen). For antigen-specific $CD8^+$ T cell activation, OT-I or P14 splenocytes were treated with 1 µg ml^{-1} OVA257-264 or gp33 peptides in the presence of 10 ng ml^{-1} IL-2 for 3 days, then cultured with IL-2 alone for another 3 days before adoptive transfer or *in vitro* assays. For human $CD8^+$ T cells, blood was drawn from healthy donors according to the guidelines of ethic regulation under approved protocol at University of Lausanne (protocol P_173) with written informed consent. PBMCs were isolated by Ficoll gradient. $CD8^+$ T cells were then isolated from PBMCs using negative selection Mojosort kit (BioLegend). Isolated $CD8^+$ T cells were resuspended with medium containing 10 ng ml^{-1} human IL-2 (Peprotech) and then activated with Dynabeads Human T-Activator CD3/CD28 (Gibco). Throughout expansion, the cell concentration was maintained between 0.5 –1.0 × 10^6 cells per ml. Cells were further used for following experiments between day 15 to day 17 post-activation.

Tumor digestion, cell isolation and FACS analysis

Tumors were minced in RPMI with 2% FBS, DNaseI (1 µg ml^{-1}, Sigma-Aldrich) and collagenase (0.5 mg ml^{-1}, Sigma-Aldrich), followed by digesting at 37°C for 45 min. The digested samples were then filtered through a 70-µm cell strainer, enriched by density gradient centrifugation (800*g*, 30 min) at 25°C with 40% and 80% percoll (GE Healthcare). FACS analyses were performed using LSRII (BD Biosciences) with BD FACSDiva software (version 8.0.1). Data were analyzed using FlowJo. For MitoTracker staining, cells were incubated with 10 nM MitoTracker Deep Red (Thermo Fisher Scientific) and 100 nM MitoTracker Green (Thermo Fisher Scientific) in RPMI with 2% FBS for 15 min at 37°C for mitochondrial membrane potential and mass, respectively. For cytokine examination, cells were stimulated with either OVA or gp33 peptides in the presence of brefeldin A (5 ng ml^{-1}) for 5 h and then stained by the intracellular staining procedure as described [3]. The following antibodies were used: anti-CD3ε (ebioscience, 1:300), anti-CD4 (ebioscience, 1:100), anti-CD8a (ebioscience, 1:100), anti-CD44 (ebioscience, 1:300), anti-CD45.1 (BioLegend, 1:50), anti-CD45.2 (BioLegend, 1:100), anti-CD90.1

(ebioscience, 1:1000), anti-PD-1 (BioLegend, 1:200), anti-T-bet (ebioscience, 1:200), anti–TCF1 (Cell signaling, 1:100), anti-IFN-γ (BioLegend, 1:1000), anti-TNF (BioLegend, 1:200), anti-LAG3 (BioLegend, 1:200), anti-hCD3 (BioLegend, 1:100), anti-hCD8 (BioLegend, 1:100), anti-hCD45RA (BioLegend, 1:100)

TCR clonality in human patient samples

Human samples were collected according to the guidelines of ethic regulation under approved protocols at University Hospital Basel (EK128/13) and Lausanne University Hospital (protocol 87/06). Human PBMCs were collected according to the approval protocol at University of Lausanne (A150519/2) Written informed consent was obtained from all participants. MDR/MG^{hi} and MDR/MG^{lo} CD8^{+} TILs were analyzed from tumor infiltrated lymph nodes (TILNs) from melanoma patients and human colon cancer samples (**Extended Data Table 1**). Subsequently, sorted MDR/MG^{hi} and MDR/MG^{lo} CD8^{+} TILs from human colon cancer were further resuspended with lysis buffer, followed by the RNAseq analysis for TCR b-chain. A clonality score was determined by the Simpson index.

Electron microscopy, tomography and 3D structural analysis of mitochondrial morphology

For Electron microscopy analysis, sorted cells were fixed in glutaraldehyde solution (EMS,) 2.5% for 1 h at 25°C, and directly postfixed with osmium tetroxide 1% (EMS)/1.5% of potassium ferrocyanide (Sigma) for 1 h at 25°C, followed by several washes and dehydration in acetone (Sigma), and embedded in Epon (Sigma). Ultrathin sections of 50nm were prepared on a Leica Ultracut (Leica Mikrosysteme GmbH), followed by poststained with 4% uranyl acetate (Sigma) and Reynolds lead citrate (Sigma). Micrographs were taken with a transmission electron microscope Philips CM100 (Thermo Fisher Scientific) at an acceleration voltage of 80kV with a TVIPS TemCam-F416 digital camera (TVIPS GmbHImage) analysis and quantification were carried out using ImageJ software. The number of mitochondrion per cell was quantified. For assessing mitochondrial cristae, each dot represents the crista number or total length in one mitochondrion from one high-magnitude EM image of a live cell. For electron tomography, a hydrophilic surface was obtained by glow discharge (25 mA for 10 sec) on the slot grids (2 × 0.5 mm oval slots) with carbon films. The fiducial markers (10 µl of diluted 10 nm gold nanoparticles with 1% BSA coating) were absorbed (10 min), blotted and air-dried on the carbon film. The serial sections (200nm in thickness) were cut and the ribbon of sections was collected by a homemade perfect loop, followed by staining with Reynold's lead citrate for 10 min. The stained and dried grids were subjected to glow discharge again and the second layer of fiducial gold was applied to the sections. The grids were loaded into the double tilt holder (Model 2040 Dual-Axis Tomography

Holder, Fischione) and imaged with FEI Tecnai TEM operating at 200 kV. The micrographs were recorded with a Gatan UltraScan 1000 CCD at 0.87 nm/pixel (9,600×) and the tilt series from − 58° to + 58° with 2° increments were acquired using the Legion automatic and remote control software. The serial tomograms with double tilt were reconstructed, combined, and joined in eTomo, while the 3D volume of the selected area was segmented and visualized in Amira [57].

Measurement of mitochondrial membrane potential and mass by FACS

T cells were treated with or without 10 μM Oligomycin A (Sigma-Aldrich) for 2.5 h, and then stained with 10 nM MitoTracker Deep Red (Thermo Fisher Scientific) and 100 nM MitoTracker Green (Thermo Fisher Scientific) for 15 min at 37^{o}C for mitochondrial membrane potential and mass, respectively. FACS analyses were performed using LSRII (BD Biosciences). Data were analyzed using FlowJo.

Determination of mitochondrial DNA copy number

Mitochondrial DNA copy number of $CD8^+$ T cells isolated from indicated tissues was determined as mentioned previously [58]. Total DNA was extracted using Genomic-tip 20/G (QIAGEN), followed by quantitative real-time RT-PCR on a LightCycler 480 Instrument II machine (Roche Life Science) using KAPA SYBR FAST qPCR Kit Master Mix (KAPA Biosystems).

Florescence confocal microscopy

Cells were collected by the BD Influx^{TM} cell sorter and allowed to adhere on glass bottom dishes coated with poly-D-lysine. Cells were kept in a humidified incubation chamber at 37°C with 5% CO_2 during live images collection by using a Leica TCS SP5, confocal spectral microscopy fitted with an HCX PL APO 63×/1.40-0.60 Oil objective. Images of mitochondria were processed and presented as using premier 3D volume rendering modes tool in Imaris (Bitplane).

Retrovirus production and transduction

For CRISPR/Cas9-mediated Drp-1-depletion experiment, Drp-1 guide RNAs (Drp1-1 gRNA, GTGACCACACCAGTTCCTCT; Drp1-2 gRNA, CCTTCCCATCAATACATCCA; Drp1-3 gRNA, TATTTGCAGCAGTGACGGCG) were cloned into our homemade pSUPER-pU6-Thy1.1 plasmid by Bbs1. For the autophagy reporter experiment, pMSCV-mCherry-EGFP-LC3B-Thy1.1 is a gift from R. Ahmed as described previously[59]. Retrovirus was produced by transfecting Phoenix cells with the indicated plasmids with pCL-Eco using TurboFect (Thermo Fisher Scientific). For $CD8^+$ T cell retrovirus transduction, activated $CD8^+$ T cells were cultured with medium containing virus and 10 ng ml^{-1} IL-2 in

the retronectin (Takara Bio Europe)-coated plates. The following experiments were performed 5 days after transduction.

RNA-seq data processing and computational analysis

mRNA-seq profiling using the Smart-seq2 protocol was performed as described previously[60]. Smart-seq2 reads were trimmed using *Trimmomatic* (v.0.32)[61] and mapped to the mouse reference genome (mm10) using STAR (v.2.5.2b)[62]. *summarizeOverlaps* from the GenomicAlignments package (v.1.16.0) in R/Bioconductor (v.3.5.1) was used to quantify gene expression by counting primary alignments to exons. Genes were defined using Ensembl annotation of mm10/GRCm38 (genome-build GRCm38.p6). Differential expression analysis was performed using DESeq2 (v.1.22.2)[63].

ATAC-seq data processing and computational analysis

T cells from indicated conditions were collected and performed chromatin accessibility mapping by ATAC-seq as described previously[64]. Raw reads were trimmed using *Trimmomatic* (v.0.32)[61] and aligned to the mouse reference genome (mm10) using Bowtie2 (v.2.2.4)[65]. Duplicate reads were removed using sambamba (v.0.5.5)[66] and only primary alignments with mapping quality greater than 30 were retained. Genome browser tracks were generated using BEDTools (v.2.26.0)[67] and the UCSC Genome Browser's *bedGraphToBigWig* tool. ATAC-seq peaks were called using MACS2 (v.2.1.1.20160309)[68] on each individual sample. Peaks overlapping with blacklisted regions (http://mitra.stanford.edu/kundaje/akundaje/release/blacklists/mm10-mouse/) were discarded. Peaks from all samples were merged into a consensus peak list using BEDTools *merge.* The chromatin accessibility of each consensus peak in each sample was quantified using BEDTools *coverageBed*. Differential accessibility was calculated using *DESeq2* (v.1.22.2)[63]. Differentially accessible regions between populations were defined using adjusted P-value ≤ 0.05 and $|\log_2(\text{fold-change})| \geq 0.5$ for *in vivo* experiments, P-value ≤ 0.05 and $|\log_2(\text{fold-change})| \geq 0.5$ for *in vitro* experiments. The distribution of differentially accessible regions was calculated using PAVIS[69]. For Figure 4a, ATAC values were normalized using *vst* from *DESeq2*, followed by row-median normalization. The QC table for ATCA-seq of *in vivo* (**Extended Table 4**) and *in vitro* TILs (**Extended Table 6**) is available in supplementary information. The differentially accessible chromatin loci of *in vivo* (**Extended Table 5**) and *in vitro* TILs (**Extended Table 7**) can be found in supplementary information.

Gene set enrichment analysis

Enrichment of manually curated gene sets was calculated by GSEA (v.3.0)[70] using the pre-ranked analysis option. For Figure 3e-f, mouse gene IDs were mapped to human gene names using the Ensembl/Biomart

941 database using *biomaRt* (v.2.38.0). *DEseq2* $\log_2$(fold-change) expression values were used to rank the
942 genes. For Figure 4c, peaks were assigned to the closest transcription start sites using the BEDTools
943 *closestBed*, subsequently mouse gene symbols were mapped to human gene symbols using *biomaRt*. The
944 *DESeq2* $\log_2$(fold-change) accessibility values were used to rank the genes. The $\log_2$(fold-change) with
945 the highest absolute value was selected if more than one peak was assigned to a gene. For Figure 7f, the
946 consensus list of *in vivo* peaks ranked according to their differential accessibility contrasting two
947 populations ($\log_2$(fold-change) values) was compared to sets of differentially accessible peaks defined *in*
948 *vitro*. The *in vitro* peaks were assigned to the closest *in vivo* peaks using the BEDTools *closestBed.*
949
950 **Whole-genome bisulfite sequencing (WGBS)**
951 T cells from indicated conditions were collected for the WGBS as described previously[71], with minor
952 adaptations. Bisulfite conversion was performed using the EZ DNA Methylation-Direct Kit (Zymo
953 Research, D5020) with the modification of eluting the DNA in only 9µl of elution buffer. Bisulfite
954 treatment was performed directly on lysed cells by placing the cells in digestion buffer and performing
955 proteinase K digestion at 50°C for 20min. In both cases, custom-designed methylated and unmethylated
956 oligonucleotides were added at a concentration of 0.1% to serve as spike-in controls for monitoring
957 bisulfite conversion efficiency. Libraries for next-generation sequencing were prepared using the
958 TruSeq® DNA Methylation Kit (Illumina, EGMK91396) with the following critical steps: bisulfite-
959 converted genomic DNA was transcribed using tagged random hexamer primers, excess random hexamer
960 primers were digested by the addition of Exonuclease I, terminal tagging was performed to extend the
961 synthesized DNA strand on its 3′ side using elongation blocked and tagged random hexamers, and
962 Illumina-compatible sequencing adapters were introduced through enrichment PCR using primers
963 corresponding to the tagged sequences flanking the random hexamers. For subsequent library
964 amplification, the number of PCR cycles was 14 cycles, adjusted according to cell number. The final
965 library was purified twice using Agencourt AMPure XP beads (Beckman Coulter, A63880). Quality
966 control for the final library was performed by measuring the DNA concentration with the QuBit dsDNA
967 HS assay (Life Technologies, Q32851) on QuBit 2.0 Fluorometer (Life Technologies, Q32866) and by
968 determining library fragment sizes with the Bioanalyzer High Sensitivity DNA Kit (Agilent, 5067-4626).
969
970 **WGBS data processing and normalization**
971 Bisulfite alignment of the WGBS reads to the mm10/GRCm38 assembly of the mouse reference genome
972 and methylation calling was performed using *gemBS* (v.3.3.0)[72]. The methylation beta-values were
973 calculated using *RnBeads*[73]. Sites exhibiting differential DNA methylation between populations were
974 identified using *limma* as implemented in *RnBeads*. Hypermethylated and hypomethylated regions

between MDR/MG^{hi} and MDR/MG^{lo} populations were defined using adjusted P-value ≤ 0.05 and |$\log_2$(quotient of mean DNA methylation levels)|≥0.5. The distribution of differentially methylated regions was calculated using PAVIS[69]. The QC table (**Extended Table 2**) and the differentially methylated regions (**Extended Table 3**) for WGBS-seq of *in vivo* TILs is available in supplementary information.

Identifying TF binding motifs

To identify TF-binding motifs enriched in the sets of accessible (or methylated) regions, we used *i-cisTarget* (online v.5.0, input bed files, genome mm9, 20003 PWMs)[74]. The UCSC *liftover* tool was used to convert analyzed regions from mm10 to mm9. Predicted target regions from the same motif cluster were merged. TFs expressed in our RNA data and annotated for binding enriched motifs specifically in MDR/MG^{hi} or MDR/MG^{lo} were assigned.

Pathway enrichment analysis

Pathway analysis was performed with *Enrichr*[75] where genes assigned to sets of differentially accessible or methylated regions were compared to genesets from NCI-Nature 2016 Pathway database.

Examination of mitochondrial fitness with *in vitro* treatments

For TCM/TCR/Hypoxia experiment, *in vitro*-activated CD8$^+$ T cells were cultured with YUMM1.7 melanoma conditional medium in the presence of Dynabeads Mouse T-Activator CD3/CD28 (Gibco) under hypoxia condition (1.0% O_2) w/ or w/o 10 mM glucose. For mitochondrial uncouplers treatments, *in vitro*-activated CD8$^+$ T cells were cultured in medium either with 10 μM oligomycin/1 μM antimycin A (Sigma-Aldrich) for 4 h or 10 μM oligomycin/200 μM Mdivi-1 for 6 h. For improvement of mitochondrial fitness, *in vitro*-activated CD8$^+$ T cells were cultured under TCM/TCR/Hypoxia condition with 400 μM NR or 50 μM MitoTempo (Sigma-Aldrich).

RNA extraction, RT-PCR and qPCR

In vitro-activated CD8$^+$ T cells upon indicated treatments were collected. RNAs were then extracted using TRIzol reagent (Life Technologies). Complementary DNA was converted from mRNA using M-MLV Reverse Transcriptase (Promega). Indicated mRNA expression was performed in triplicate by quantitative real-time RT-PCR on a LightCycler 480 Instrument II machine (Roche Life Science) using KAPA SYBR FAST qPCR Kit Master Mix (KAPA Biosystems). Relative expression was normalized by the expression of *Actb* in each sample.

Single cell RNA-seq data analysis for hypoxia-related gene signature

Two processed scRNA-seq datasets for melanoma[50, 76] were obtained from Gene Expression Omnibus (GEO; https://www.ncbi.nlm.nih.gov/gds) under accession numbers GSE72056 and GSE115978. The deconvolution method[77] implemented in was applied to normalize the read counts among cells. The read count for each gene was computed by multiplying the TPM value and gene length (for gene with multiple transcripts, the length of the longest transcript was used). Normalized gene counts were finally transformed back to TPM by dividing the gene lengths. The gene expression levels were quantified as the log2(TPM +1) for the following analysis. For analysis of the four states of $CD8^+$ T cells, $CD8^+$ T cells were classified as non-exhausted (*PDCD1*$^-$, *PRDM1*$^+$, *KLRG*$^+$) and exhausted (*PDCD1*$^+$) cells. Then, among exhausted population, we subsequently defined the *TCF7*$^+$*HAVCR2*$^-$ as the progenitor exhausted cells. The other exhausted cells with *TCF7*-low and *HAVCR2*-high were further ranked from low to high on basis of the average expression level of *HAVCR2, LAG3 and CTLA4*. The cells ranked between 35%-65% were defined as the partially exhausted cells, while the cells ranked above 70% were defined as the fully exhausted cells. The evaluation of the hypoxia status with the gene set (from https://reactome.org/content/detail/R-HSA-1234174) was further conducted among four states of $CD8^+$ cells. The Mann-Whitney test were applied to assess significant differences between fully exhausted cells and other cell populations.

Statistical analysis

Data points represent biological replicates and are shown as mean ± s.e.m. or mean ± s.d. as mentioned in the figure legends. Statistical significance was determined as indicated in the figure legends. Wilcoxon matched-pairs signed rank test was applied to determine statistical differences of TCR clonality between MDR/MG^{hi} and MDR/MG^{lo} population isolated from human colon cancer. Other data were analyzed using two-tailed, unpaired/paired, Student's *t*-test as mentioned in the figure legends.

Reporting Summary. Detailed information on experimental design is available in the Life Sciences Reporting Summary linked to this article.

Data availability

The Smart-seq2, ATAC-seq and WGBS data are available in the Gene Expression Omnibus database under accession code (ATAC-seq: GSE144582; WGBS: GSE144583; RNA-seq: GSE156506). The data analysis code is available at https://github.com/himrichova/CD8_TIL_exhaustion. Processed data are, furthermore, publicly available in the UCSC Genome Browser using the following link: http://genome-euro.ucsc.edu/s/himrichova/CD8_TIL_exhaustion_mm10. All the information and data are summarized

and available at https://www.medical-epigenomics.org/papers/Yu2020/#home. Other relevant data are available from the corresponding author upon request.

Methods-only References

51. Shin, J.H. *et al.* PARIS (ZNF746) repression of PGC-1alpha contributes to neurodegeneration in Parkinson's disease. *Cell* **144**, 689-702 (2011).

52. Pan, H., Zhang, C., Wang, T., Chen, J. & Sun, S.K. In Situ Fabrication of Intelligent Photothermal Indocyanine Green-Alginate Hydrogel for Localized Tumor Ablation. *ACS Appl Mater Interfaces* **11**, 2782-2789 (2019).

53. Chao, Y. *et al.* Combined local immunostimulatory radioisotope therapy and systemic immune checkpoint blockade imparts potent antitumour responses. *Nat Biomed Eng* **2**, 611-621 (2018).

54. Hayashi, K., Sakamoto, W. & Yogo, T. Smart Ferrofluid with Quick Gel Transformation in Tumors for MRI-Guided Local Magnetic Thermochemotherapy. *Adv Funct Mater* **26**, 1708-1718 (2016).

55. Ho, P.C. *et al.* Immune-based antitumor effects of BRAF inhibitors rely on signaling by CD40L and IFNgamma. *Cancer Res* **74**, 3205-3217 (2014).

56. Meeth, K., Wang, J.X., Micevic, G., Damsky, W. & Bosenberg, M.W. The YUMM lines: a series of congenic mouse melanoma cell lines with defined genetic alterations. *Pigment Cell Melanoma Res* **29**, 590-597 (2016).

57. Jiang, Y.F., Lin, H.L. & Fu, C.Y. 3D Mitochondrial Ultrastructure of Drosophila Indirect Flight Muscle Revealed by Serial-section Electron Tomography. *J Vis Exp* (2017).

58. Rooney, J.P. *et al.* PCR based determination of mitochondrial DNA copy number in multiple species. *Methods Mol Biol* **1241**, 23-38 (2015).

59. Xu, X.J. *et al.* Autophagy is essential for effector CD8(+) T cell survival and memory formation. *Nature Immunology* **15**, 1152-1161 (2014).

60. Picelli, S. *et al.* Full-length RNA-seq from single cells using Smart-seq2. *Nat Protoc* **9**, 171-181 (2014).

61. Bolger, A.M., Lohse, M. & Usadel, B. Trimmomatic: a flexible trimmer for Illumina sequence data. *Bioinformatics* **30**, 2114-2120 (2014).

62. Dobin, A. *et al.* STAR: ultrafast universal RNA-seq aligner. *Bioinformatics* **29**, 15-21 (2013).

63. Love, M.I., Huber, W. & Anders, S. Moderated estimation of fold change and dispersion for RNA-seq data with DESeq2. *Genome Biol* **15**, 550 (2014).

64. Rendeiro, A.F. *et al.* Chromatin accessibility maps of chronic lymphocytic leukaemia identify subtype-specific epigenome signatures and transcription regulatory networks. *Nat Commun* **7**, 11938 (2016).

65. Langmead, B. & Salzberg, S.L. Fast gapped-read alignment with Bowtie 2. *Nat Methods* **9**, 357-U354 (2012).

66. Tarasov, A., Vilella, A.J., Cuppen, E., Nijman, I.J. & Prins, P. Sambamba: fast processing of NGS alignment formats. *Bioinformatics* **31**, 2032-2034 (2015).

67. Quinlan, A.R. & Hall, I.M. BEDTools: a flexible suite of utilities for comparing genomic features. *Bioinformatics* **26**, 841-842 (2010).

68. Zhang, Y. *et al.* Model-based analysis of ChIP-Seq (MACS). *Genome Biol* **9**, R137 (2008).

69. Huang, W., Loganantharaj, R., Schroeder, B., Fargo, D. & Li, L. PAVIS: a tool for Peak Annotation and Visualization. *Bioinformatics* **29**, 3097-3099 (2013).

70. Subramanian, A. *et al.* Gene set enrichment analysis: a knowledge-based approach for interpreting genome-wide expression profiles. *Proc Natl Acad Sci U S A* **102**, 15545-15550 (2005).

71. Farlik, M. *et al.* Single-cell DNA methylome sequencing and bioinformatic inference of epigenomic cell-state dynamics. *Cell Rep* **10**, 1386-1397 (2015).

72. Merkel, A. *et al.* gemBS: high throughput processing for DNA methylation data from bisulfite sequencing. *Bioinformatics* **35**, 737-742 (2018).

73. Assenov, Y. *et al.* Comprehensive analysis of DNA methylation data with RnBeads. *Nat Methods* **11**, 1138-1140 (2014).

74. Imrichova, H., Hulselmans, G., Atak, Z.K., Potier, D. & Aerts, S. i-cisTarget 2015 update: generalized cis-regulatory enrichment analysis in human, mouse and fly. *Nucleic Acids Res* **43**, W57-64 (2015).

75. Kuleshov, M.V. *et al.* Enrichr: a comprehensive gene set enrichment analysis web server 2016 update. *Nucleic Acids Res* **44**, W90-97 (2016).

76. Jerby-Arnon, L. *et al.* A Cancer Cell Program Promotes T Cell Exclusion and Resistance to Checkpoint Blockade. *Cell* **175**, 984-997 e924 (2018).

77. Lun, A.T., Bach, K. & Marioni, J.C. Pooling across cells to normalize single-cell RNA sequencing data with many zero counts. *Genome Biol* **17**, 75 (2016).

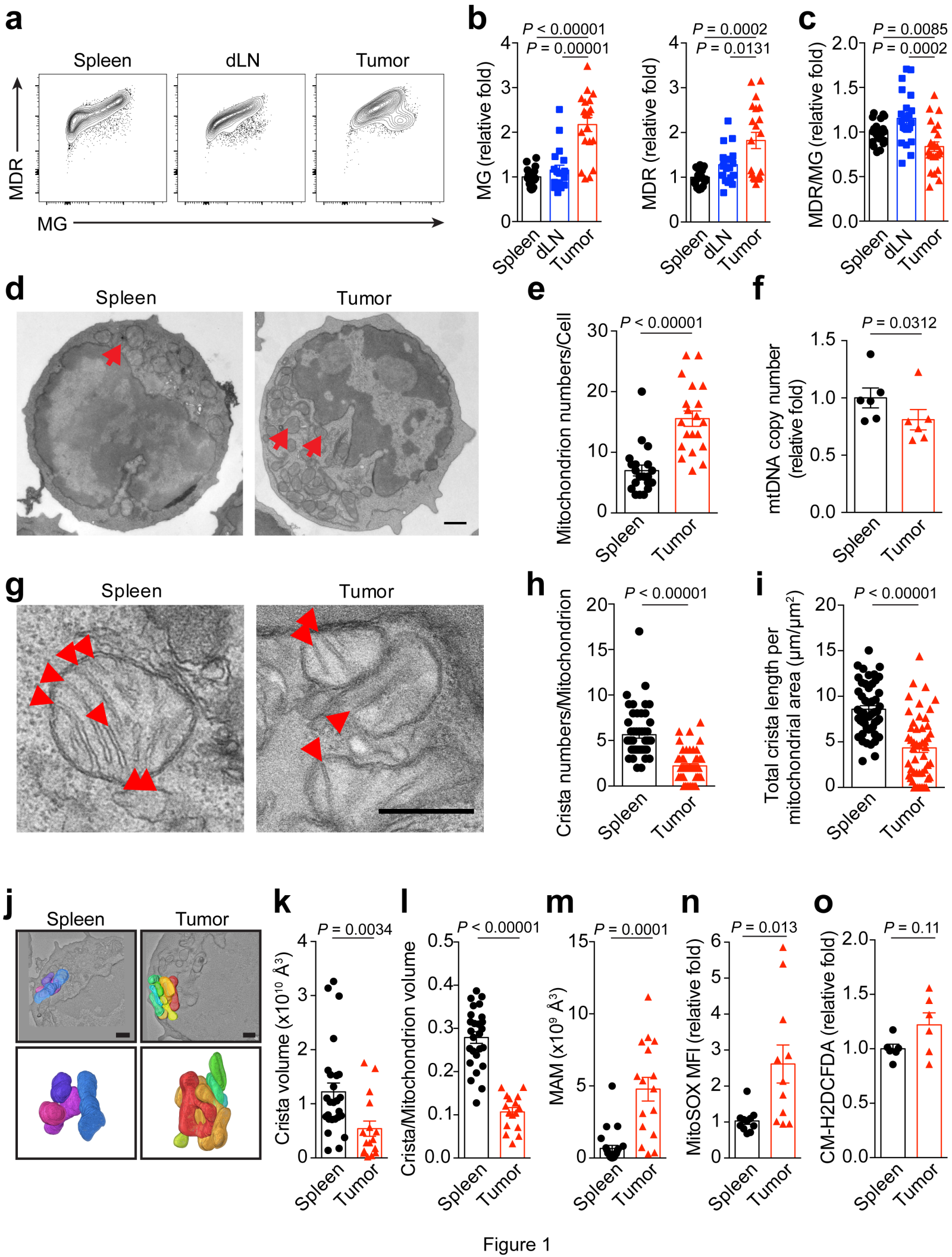
a
Spleen
dLN
Tumor
MDR
MG
b
P < 0.00001
P = 0.00001
MG (relative fold)
P = 0.0002
P = 0.0131
MDR (relative fold)
c
P = 0.0085
P = 0.0002
MDR/MG (relative fold)
Spleen
dLN
Tumor
d
Spleen
Tumor
e
P < 0.00001
Mitochondrion numbers/Cell
f
P = 0.0312
mtDNA copy number (relative fold)
g
Spleen
Tumor
h
P < 0.00001
Crista numbers/Mitochondrion
i
P < 0.00001
Total crista length per mitochondrial area (μm/μm²)
j
Spleen
Tumor
k
P = 0.0034
Crista volume (x10¹⁰ Å³)
l
P < 0.00001
Crista/Mitochondrion volume
m
P = 0.0001
MAM (x10⁹ Å³)
n
P = 0.013
MitoSOX MFI (relative fold)
o
P = 0.11
CM-H2DCFDA (relative fold)

Figure 1

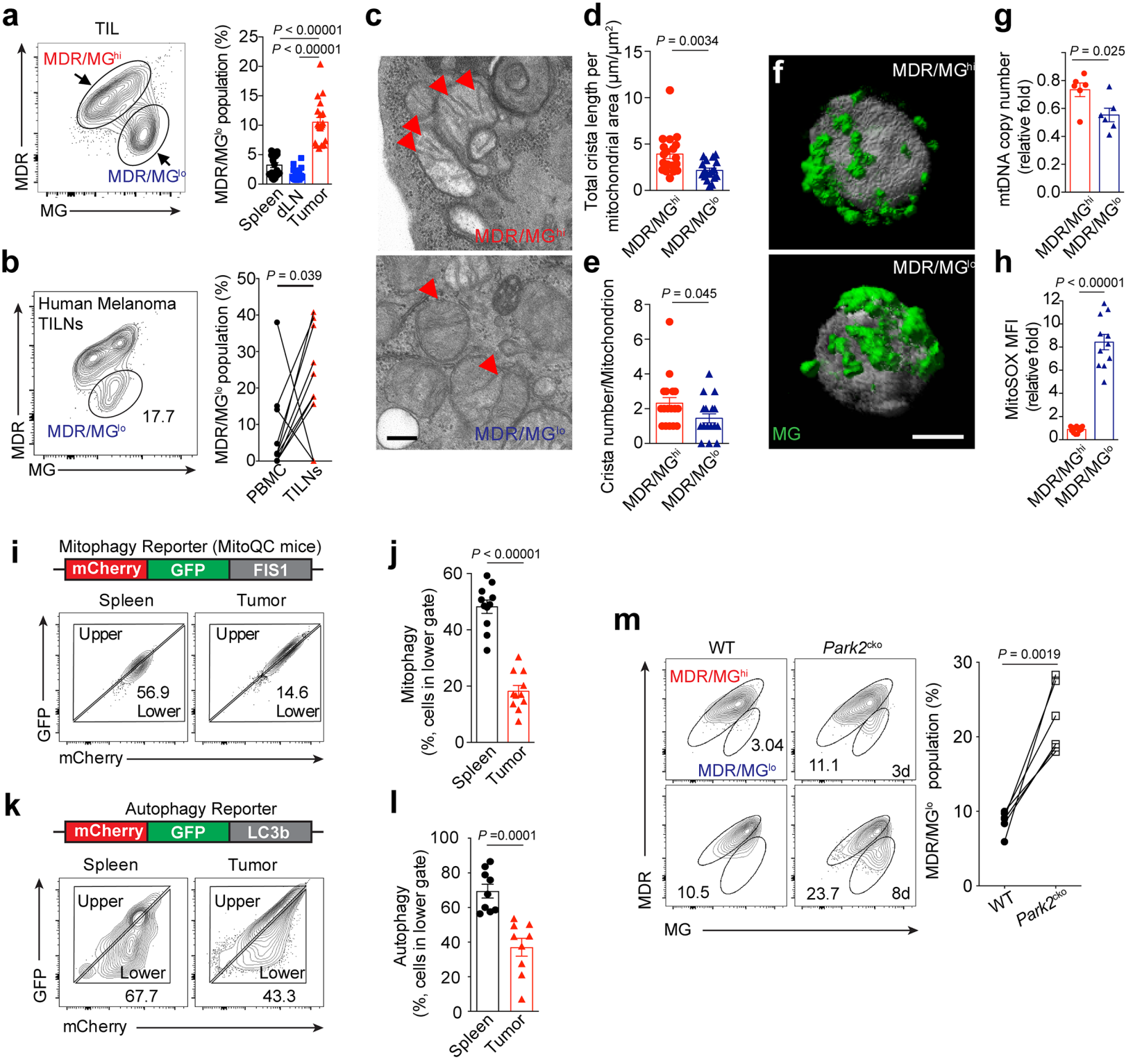
a
TIL
MDR/MG^hi
MDR/MG^lo
MDR
MG
MDR/MG^lo population (%)
P < 0.00001
P < 0.00001
Spleen
dLN
Tumor
b
Human Melanoma TILNs
17.7
MDR/MG^lo
MDR
MG
MDR/MG^lo population (%)
P = 0.039
PBMC
TILNs
c
MDR/MG^hi
MDR/MG^lo
d
Total crista length per mitochondrial area (μm/μm²)
P = 0.0034
MDR/MG^hi
MDR/MG^lo
e
Crista number/Mitochondrion
P = 0.045
MDR/MG^hi
MDR/MG^lo
f
MDR/MG^hi
MDR/MG^lo
MG
g
mtDNA copy number (relative fold)
P = 0.025
MDR/MG^hi
MDR/MG^lo
h
MitoSOX MFI (relative fold)
P < 0.00001
MDR/MG^hi
MDR/MG^lo
i
Mitophagy Reporter (MitoQC mice)
mCherry
GFP
FIS1
Spleen
Tumor
Upper
56.9
Lower
Upper
14.6
Lower
GFP
mCherry
j
Mitophagy (%, cells in lower gate)
P < 0.00001
Spleen
Tumor
k
Autophagy Reporter
mCherry
GFP
LC3b
Spleen
Tumor
Upper
Lower
67.7
Upper
Lower
43.3
GFP
mCherry
l
Autophagy (%, cells in lower gate)
P =0.0001
Spleen
Tumor
m
WT
Park2^cko
MDR/MG^hi
3.04
MDR/MG^lo
11.1
3d
10.5
23.7
8d
MDR
MG
MDR/MG^lo population (%)
P = 0.0019
WT
Park2^cko

Figure 2

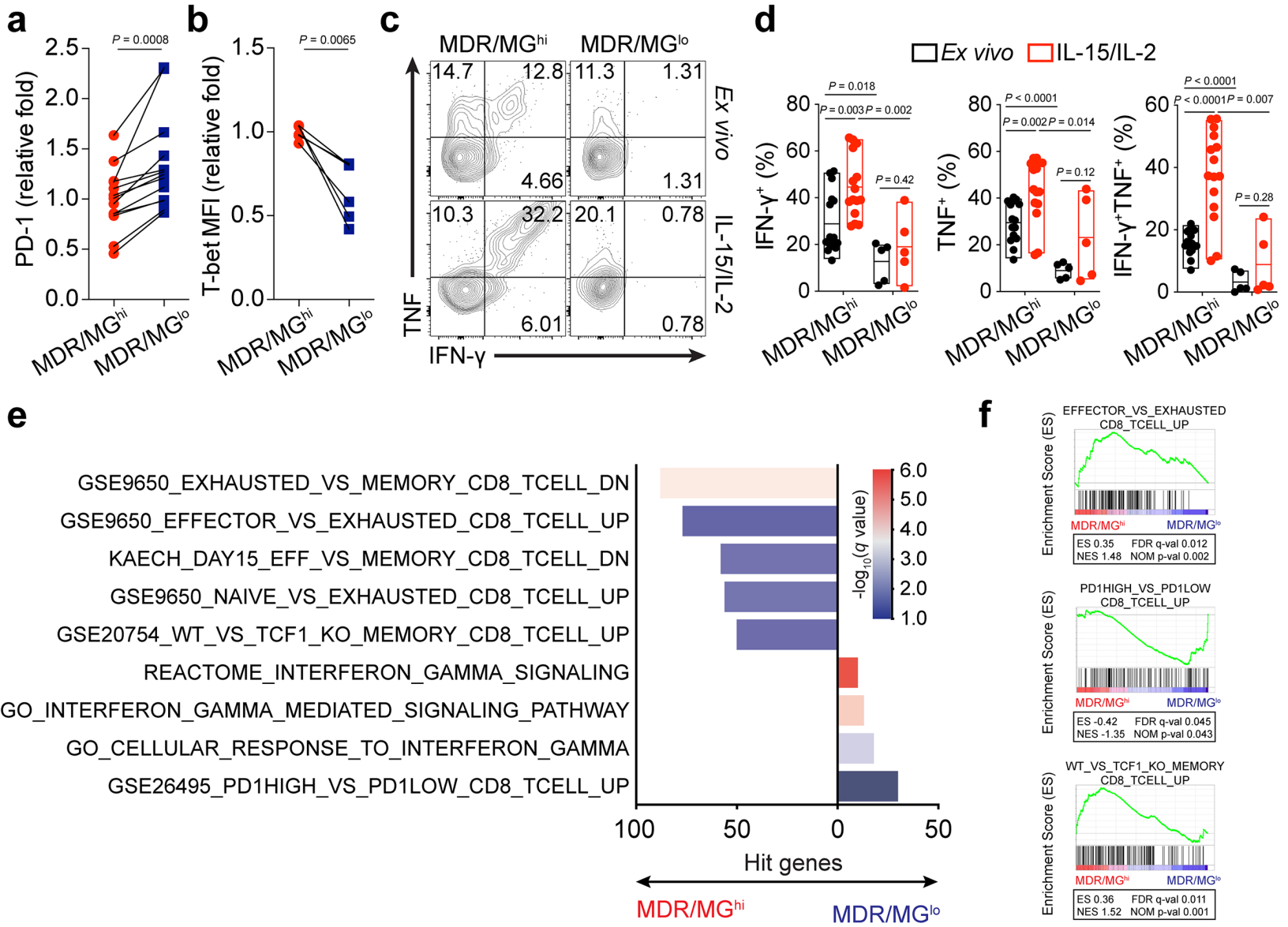
a
PD-1 (relative fold)
P = 0.0008
MDR/MGhi
MDR/MGlo
b
T-bet MFI (relative fold)
P = 0.0065
c
MDR/MGhi
MDR/MGlo
Ex vivo
IL-15/IL-2
TNF
IFN-γ
14.7
12.8
4.66
11.3
1.31
1.31
10.3
32.2
6.01
20.1
0.78
0.78
d
Ex vivo
IL-15/IL-2
IFN-γ+ (%)
TNF+ (%)
IFN-γ+TNF+ (%)
P = 0.018
P = 0.003
P = 0.002
P = 0.42
P < 0.0001
P = 0.002
P = 0.014
P = 0.12
P < 0.0001
P < 0.0001
P = 0.007
P = 0.28

e
GSE9650_EXHAUSTED_VS_MEMORY_CD8_TCELL_DN
GSE9650_EFFECTOR_VS_EXHAUSTED_CD8_TCELL_UP
KAECH_DAY15_EFF_VS_MEMORY_CD8_TCELL_DN
GSE9650_NAIVE_VS_EXHAUSTED_CD8_TCELL_UP
GSE20754_WT_VS_TCF1_KO_MEMORY_CD8_TCELL_UP
REACTOME_INTERFERON_GAMMA_SIGNALING
GO_INTERFERON_GAMMA_MEDIATED_SIGNALING_PATHWAY
GO_CELLULAR_RESPONSE_TO_INTERFERON_GAMMA
GSE26495_PD1HIGH_VS_PD1LOW_CD8_TCELL_UP
-log10(q value)
Hit genes
MDR/MGhi
MDR/MGlo

f
EFFECTOR_VS_EXHAUSTED CD8_TCELL_UP
PD1HIGH_VS_PD1LOW CD8_TCELL_UP
WT_VS_TCF1_KO_MEMORY CD8_TCELL_UP
Enrichment Score (ES)
MDR/MGhi
MDR/MGlo
ES 0.35 FDR q-val 0.012
NES 1.48 NOM p-val 0.002
ES -0.42 FDR q-val 0.045
NES -1.35 NOM p-val 0.043
ES 0.36 FDR q-val 0.011
NES 1.52 NOM p-val 0.001

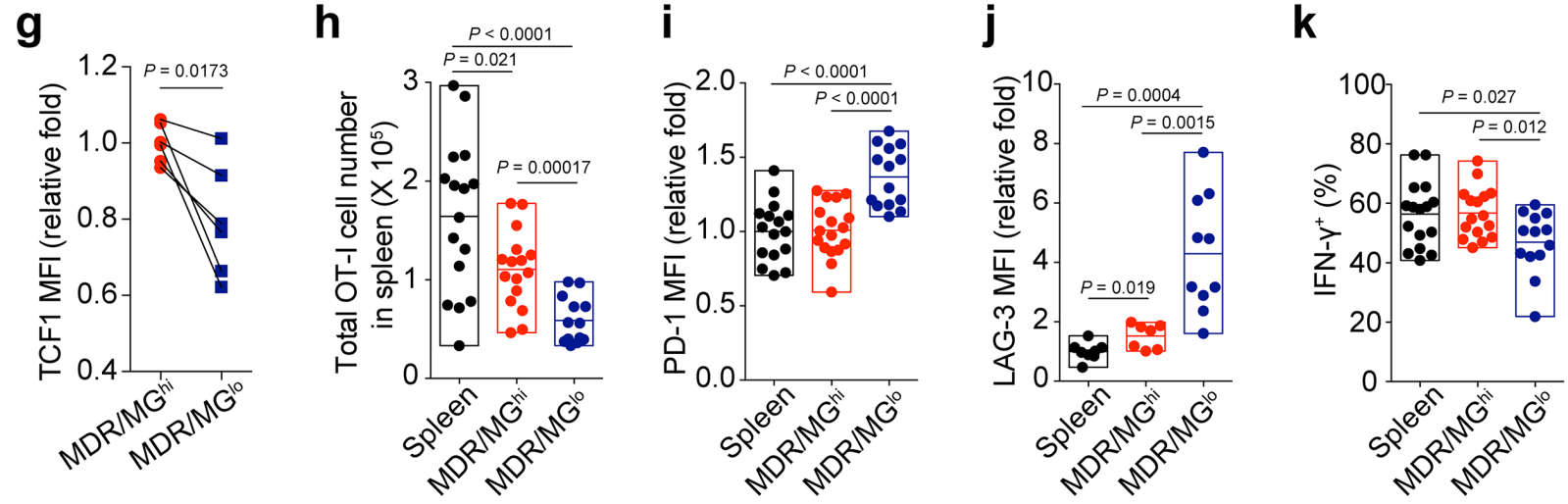
g
TCF1 MFI (relative fold)
P = 0.0173
h
Total OT-I cell number in spleen (X 10^5)
P < 0.0001
P = 0.021
P = 0.00017
i
PD-1 MFI (relative fold)
P < 0.0001
P < 0.0001
j
LAG-3 MFI (relative fold)
P = 0.0004
P = 0.0015
P = 0.019
k
IFN-γ+ (%)
P = 0.027
P = 0.012
Spleen
MDR/MGhi
MDR/MGlo

Figure 3

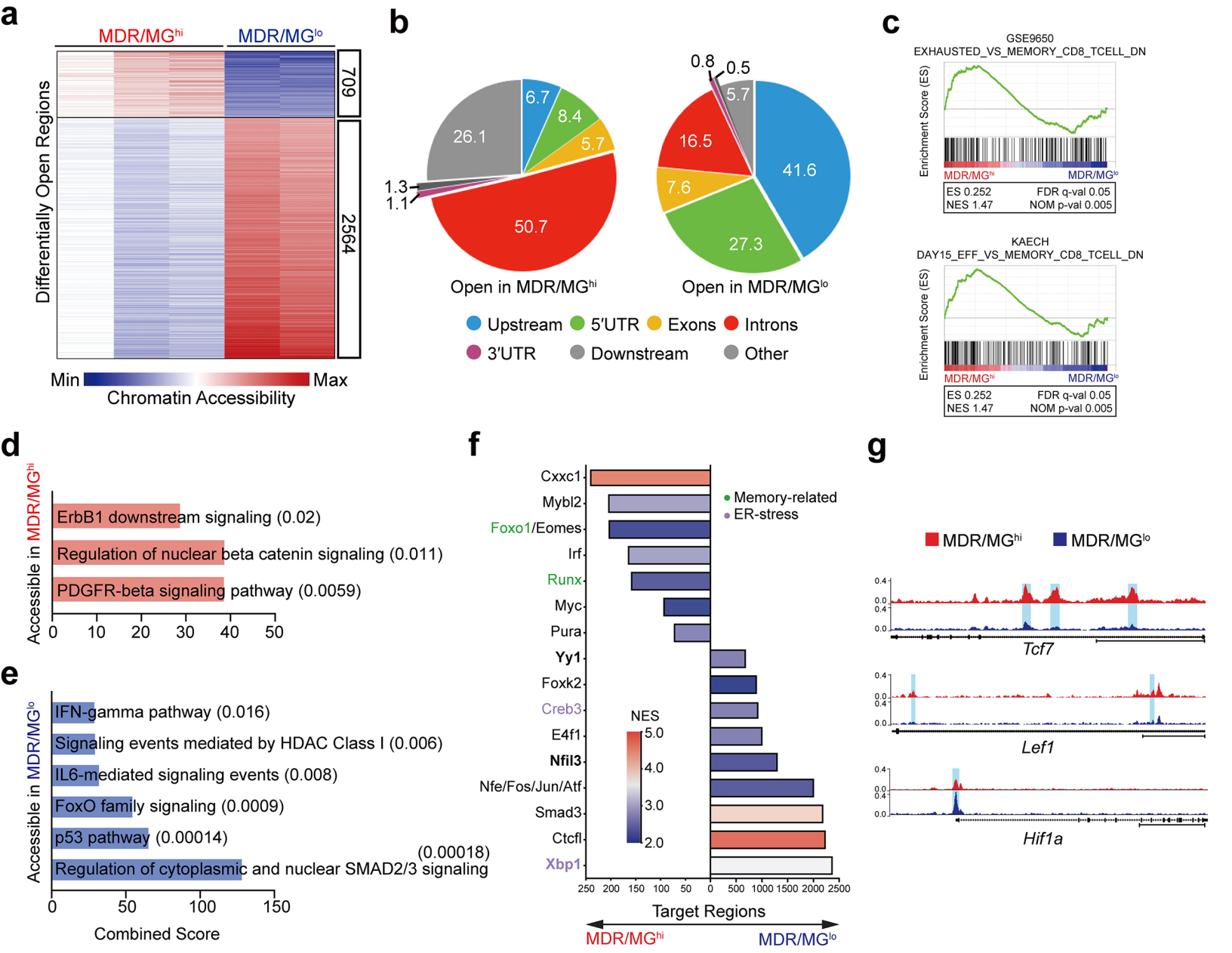
a
MDR/MG^hi
MDR/MG^lo
Differentially Open Regions
709
2564
Min
Max
Chromatin Accessibility
b
6.7
8.4
5.7
26.1
1.3
1.1
50.7
Open in MDR/MG^hi
0.8
0.5
5.7
16.5
41.6
7.6
27.3
Open in MDR/MG^lo
Upstream
5'UTR
Exons
Introns
3'UTR
Downstream
Other
c
GSE9650
EXHAUSTED_VS_MEMORY_CD8_TCELL_DN
Enrichment Score (ES)
MDR/MG^hi
MDR/MG^lo
ES 0.252
NES 1.47
FDR q-val 0.05
NOM p-val 0.005
KAECH
DAY15_EFF_VS_MEMORY_CD8_TCELL_DN
Enrichment Score (ES)
MDR/MG^hi
MDR/MG^lo
ES 0.252
NES 1.47
FDR q-val 0.05
NOM p-val 0.005
d
Accessible in MDR/MG^hi
ErbB1 downstream signaling (0.02)
Regulation of nuclear beta catenin signaling (0.011)
PDGFR-beta signaling pathway (0.0059)
0
10
20
30
40
50
e
Accessible in MDR/MG^lo
IFN-gamma pathway (0.016)
Signaling events mediated by HDAC Class I (0.006)
IL6-mediated signaling events (0.008)
FoxO family signaling (0.0009)
p53 pathway (0.00014)
Regulation of cytoplasmic and nuclear SMAD2/3 signaling (0.00018)
0
50
100
150
Combined Score
f
Cxxc1
Mybl2
Foxo1/Eomes
Irf
Runx
Myc
Pura
Yy1
Foxk2
Creb3
E4f1
Nfil3
Nfe/Fos/Jun/Atf
Smad3
Ctcfl
Xbp1
Memory-related
ER-stress
NES
5.0
4.0
3.0
2.0
250
200
150
100
50
0
500
1000
1500
2000
2500
Target Regions
MDR/MG^hi
MDR/MG^lo
g
MDR/MG^hi
MDR/MG^lo
Tcf7
Lef1
Hif1a

Figure 4

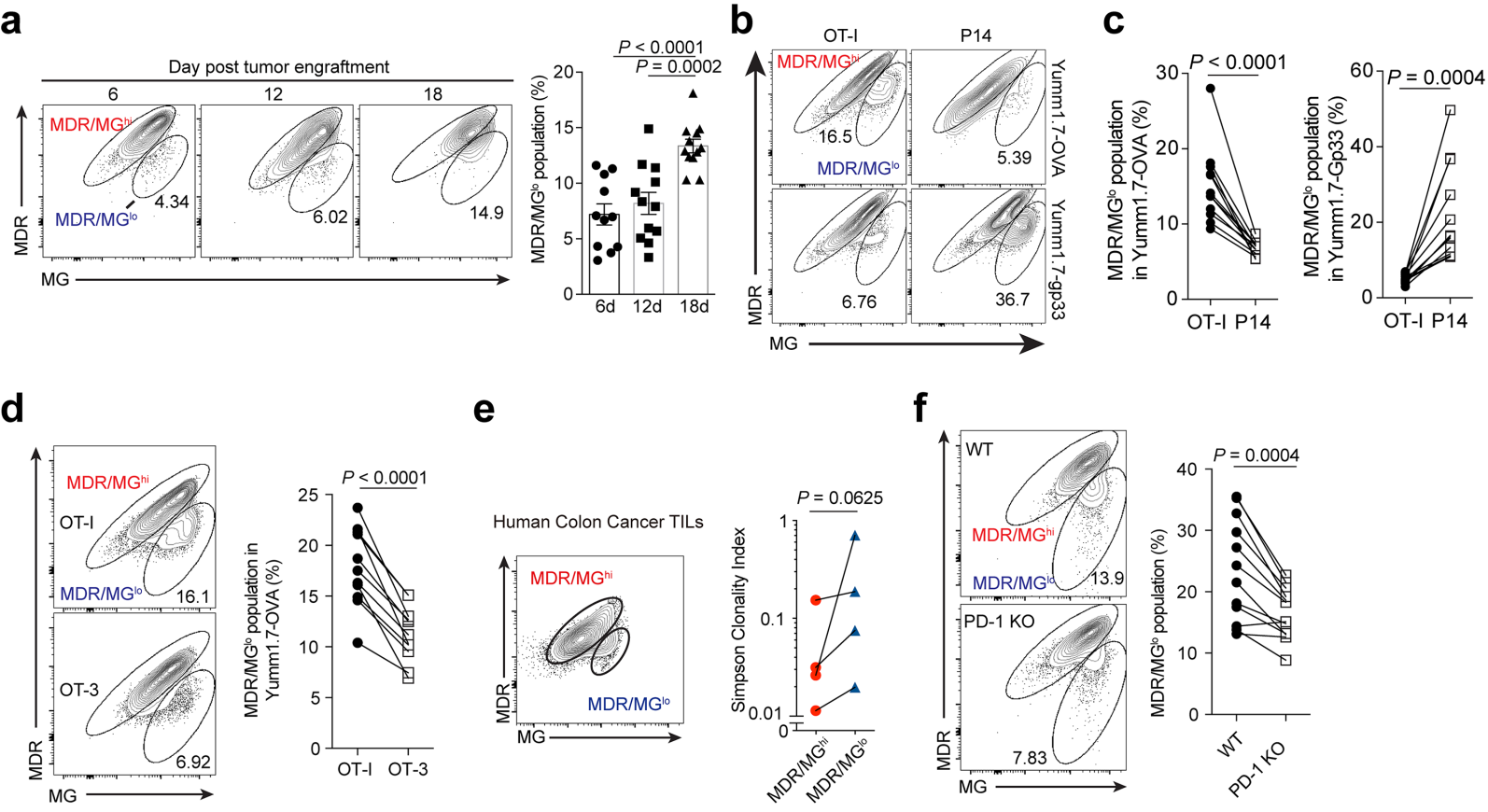
a
Day post tumor engraftment
6
12
18
MDR/MG^hi
MDR/MG^lo
4.34
6.02
14.9
MDR
MG
P < 0.0001
P = 0.0002
MDR/MG^lo population (%)
6d
12d
18d
b
OT-I
P14
MDR/MG^hi
MDR/MG^lo
16.5
5.39
6.76
36.7
Yumm1.7-OVA
Yumm1.7-gp33
MDR
MG
c
P < 0.0001
MDR/MG^lo population in Yumm1.7-OVA (%)
OT-I P14
P = 0.0004
MDR/MG^lo population in Yumm1.7-Gp33 (%)
OT-I P14
d
MDR/MG^hi
OT-I
MDR/MG^lo
16.1
OT-3
6.92
MDR
MG
P < 0.0001
MDR/MG^lo population in Yumm1.7-OVA (%)
OT-I OT-3
e
Human Colon Cancer TILs
MDR/MG^hi
MDR/MG^lo
MDR
MG
P = 0.0625
Simpson Clonality Index
MDR/MG^hi
MDR/MG^lo
f
WT
MDR/MG^hi
MDR/MG^ld
13.9
PD-1 KO
7.83
MDR
MG
P = 0.0004
MDR/MG^lo population (%)
WT
PD-1 KO

Figure 5

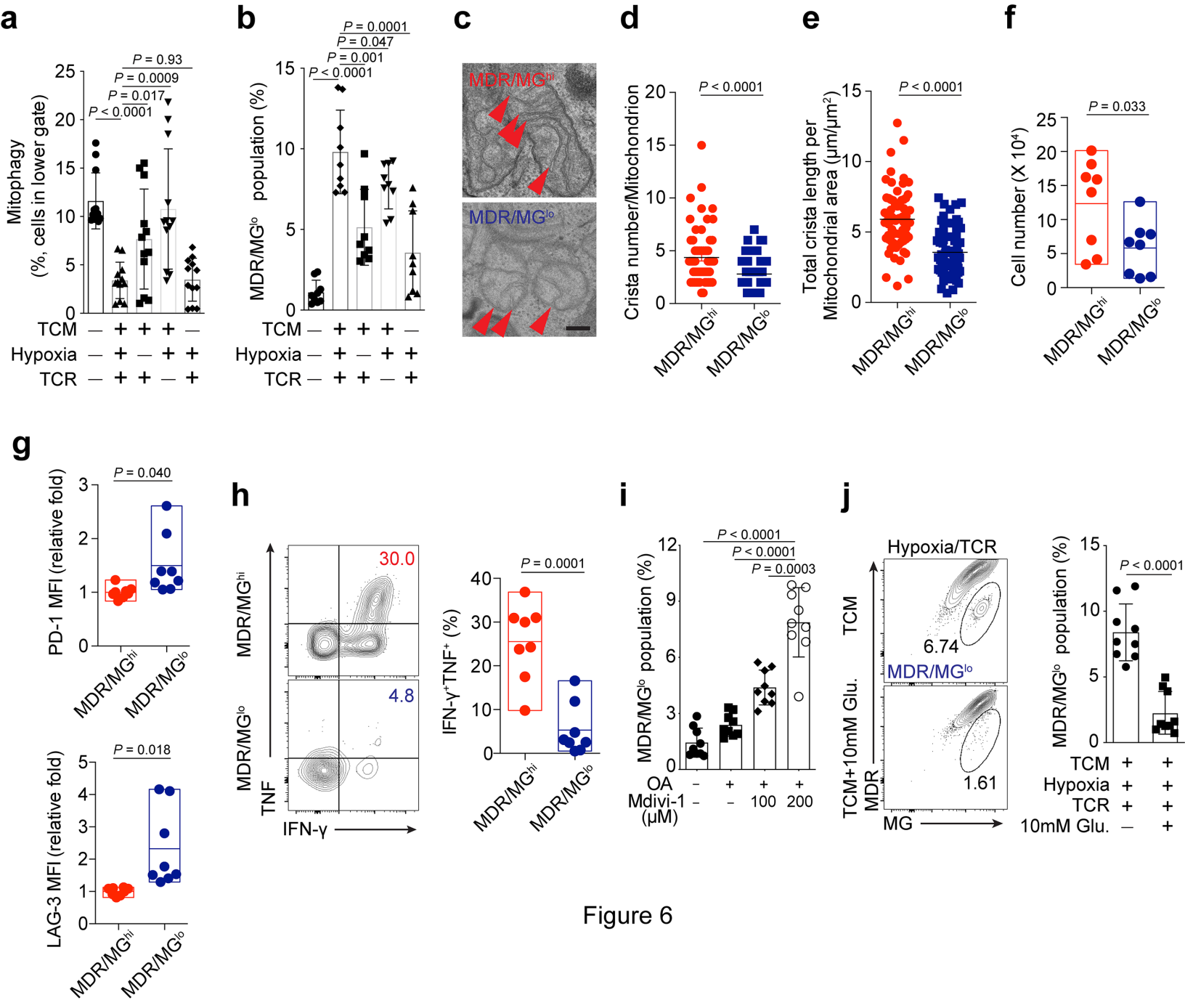
a
Mitophagy (%, cells in lower gate)
P = 0.93
P = 0.0009
P = 0.017
P < 0.0001
TCM
Hypoxia
TCR
b
MDR/MGlo population (%)
P = 0.0001
P = 0.047
P = 0.001
P < 0.0001
c
MDR/MGhi
MDR/MGlo
d
Crista number/Mitochondrion
P < 0.0001
e
Total crista length per Mitochondrial area (μm/μm2)
P < 0.0001
f
Cell number (X 10⁴)
P = 0.033
g
PD-1 MFI (relative fold)
P = 0.040
LAG-3 MFI (relative fold)
P = 0.018
h
30.0
4.8
TNF
IFN-γ
IFN-γ+TNF+ (%)
P = 0.0001
i
MDR/MGlo population (%)
P < 0.0001
P < 0.0001
P = 0.0003
OA
Mdivi-1 (μM)
j
Hypoxia/TCR
TCM
TCM+10mM Glu.
6.74
1.61
MDR
MG
MDR/MGlo population (%)
P < 0.0001
10mM Glu.

Figure 6

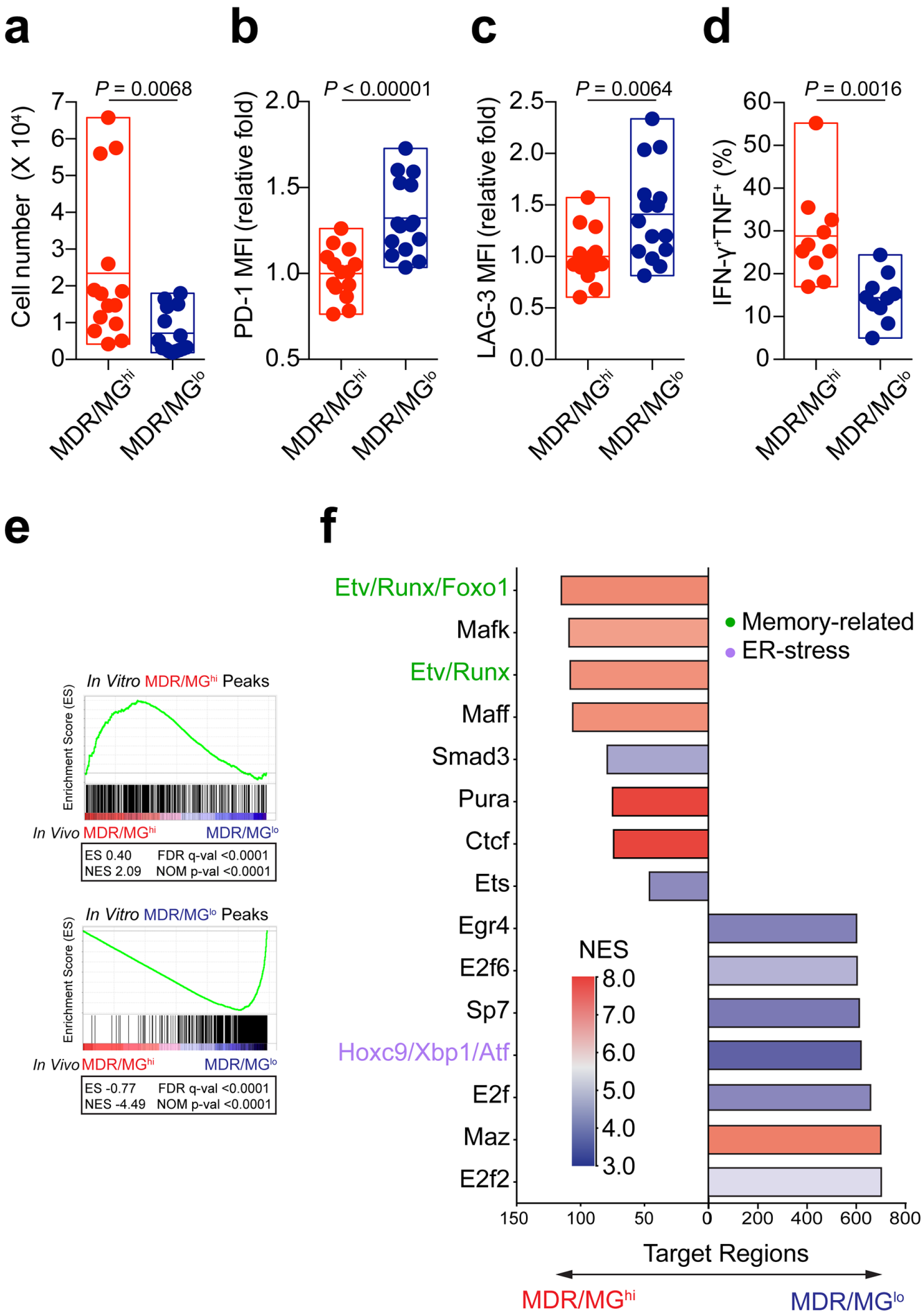
a
b
c
d
P = 0.0068
P < 0.00001
P = 0.0064
P = 0.0016
Cell number (X 10⁴)
PD-1 MFI (relative fold)
LAG-3 MFI (relative fold)
IFN-γ⁺TNF⁺ (%)
MDR/MGhi
MDR/MGlo
e
In Vitro MDR/MGhi Peaks
Enrichment Score (ES)
In Vivo MDR/MGhi
MDR/MGlo
ES 0.40
FDR q-val <0.0001
NES 2.09
NOM p-val <0.0001
In Vitro MDR/MGlo Peaks
ES -0.77
FDR q-val <0.0001
NES -4.49
NOM p-val <0.0001
f
Etv/Runx/Foxo1
Mafk
Etv/Runx
Maff
Smad3
Pura
Ctcf
Ets
Egr4
E2f6
Sp7
Hoxc9/Xbp1/Atf
E2f
Maz
E2f2
Memory-related
ER-stress
NES
Target Regions

Figure 7

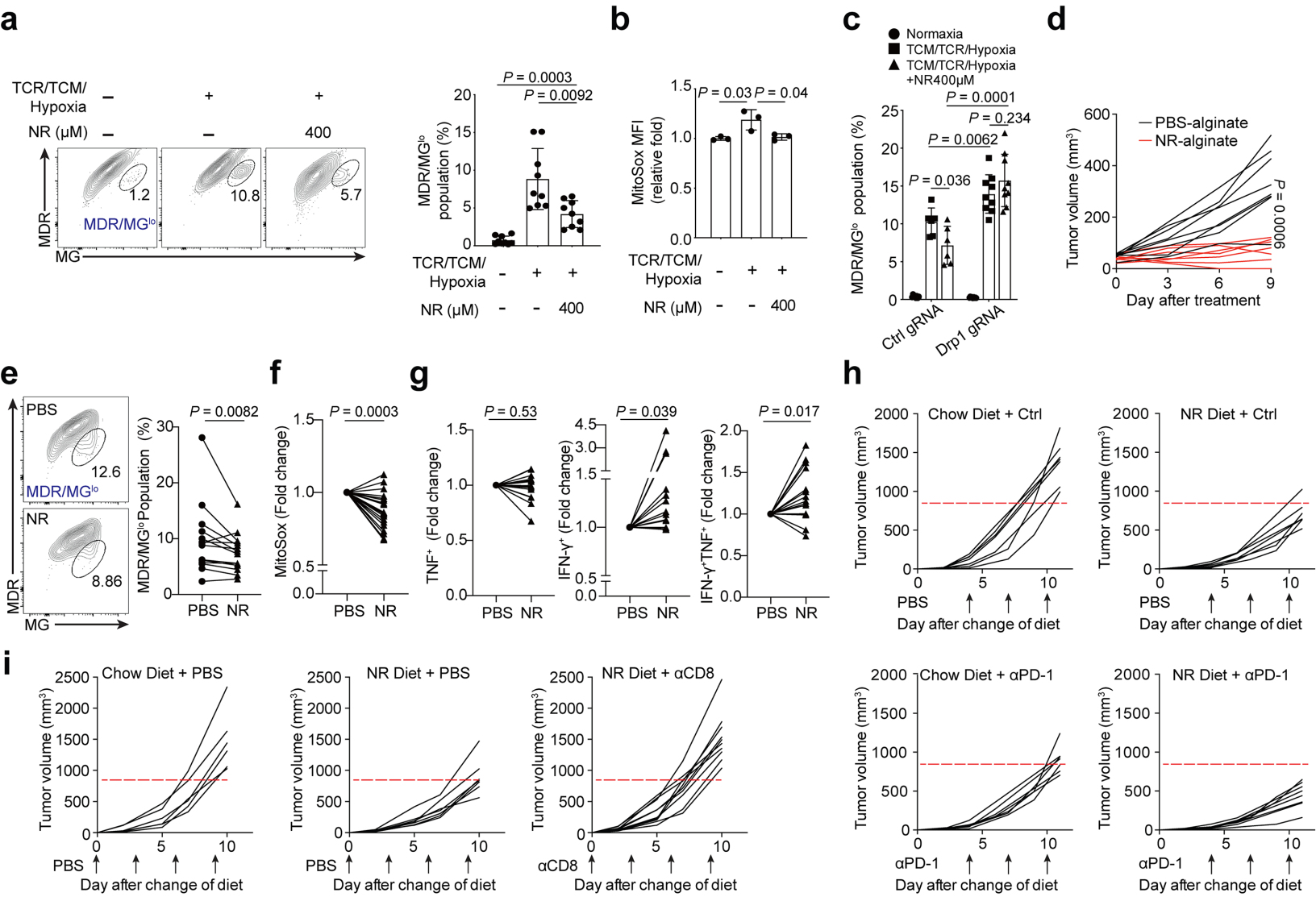
a
TCR/TCM/ Hypoxia
NR (μM)
MDR
MG
MDR/MG^lo
1.2
10.8
5.7
P = 0.0003
P = 0.0092
MDR/MG^lo population (%)
b
MitoSox MFI (relative fold)
P = 0.03
P = 0.04
c
Normaxia
TCM/TCR/Hypoxia
TCM/TCR/Hypoxia +NR400μM
P = 0.0001
P = 0.234
P = 0.0062
P = 0.036
Ctrl gRNA
Drp1 gRNA
d
PBS-alginate
NR-alginate
Tumor volume (mm3)
P = 0.0006
Day after treatment
e
PBS
NR
12.6
8.86
P = 0.0082
f
P = 0.0003
MitoSox (Fold change)
g
P = 0.53
P = 0.039
P = 0.017
TNF+ (Fold change)
IFN-γ+ (Fold change)
IFN-γ+TNF+ (Fold change)
h
Chow Diet + Ctrl
NR Diet + Ctrl
Day after change of diet
i
Chow Diet + PBS
NR Diet + PBS
NR Diet + αCD8
Chow Diet + αPD-1
NR Diet + αPD-1

Figure 8

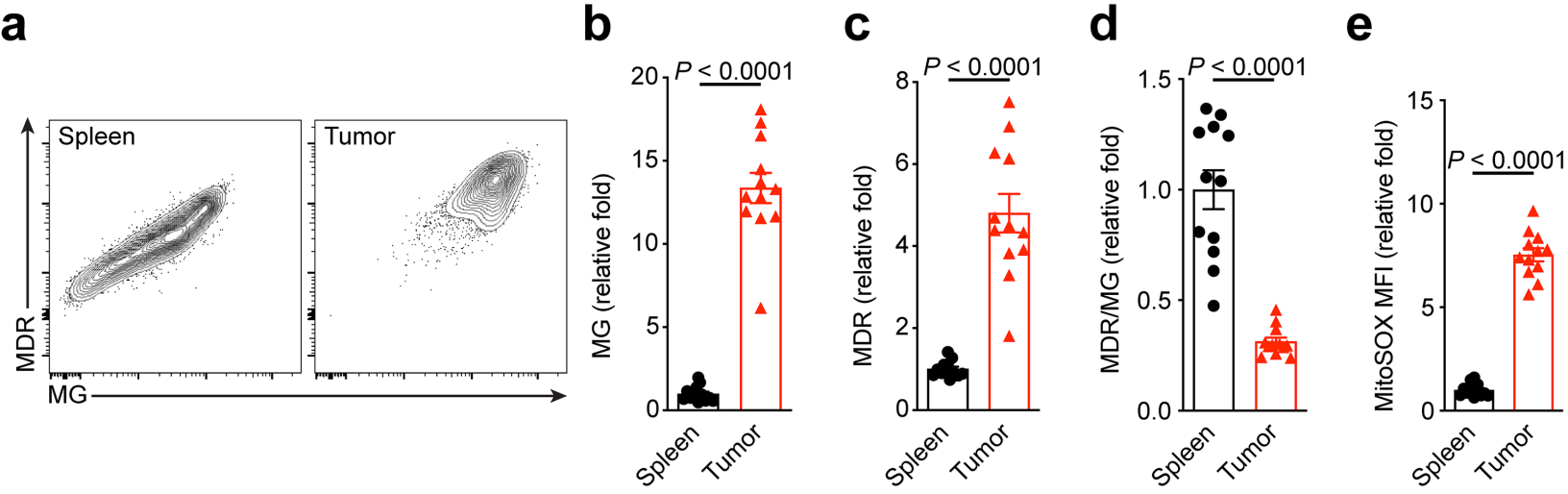

Extended Data Figure 1

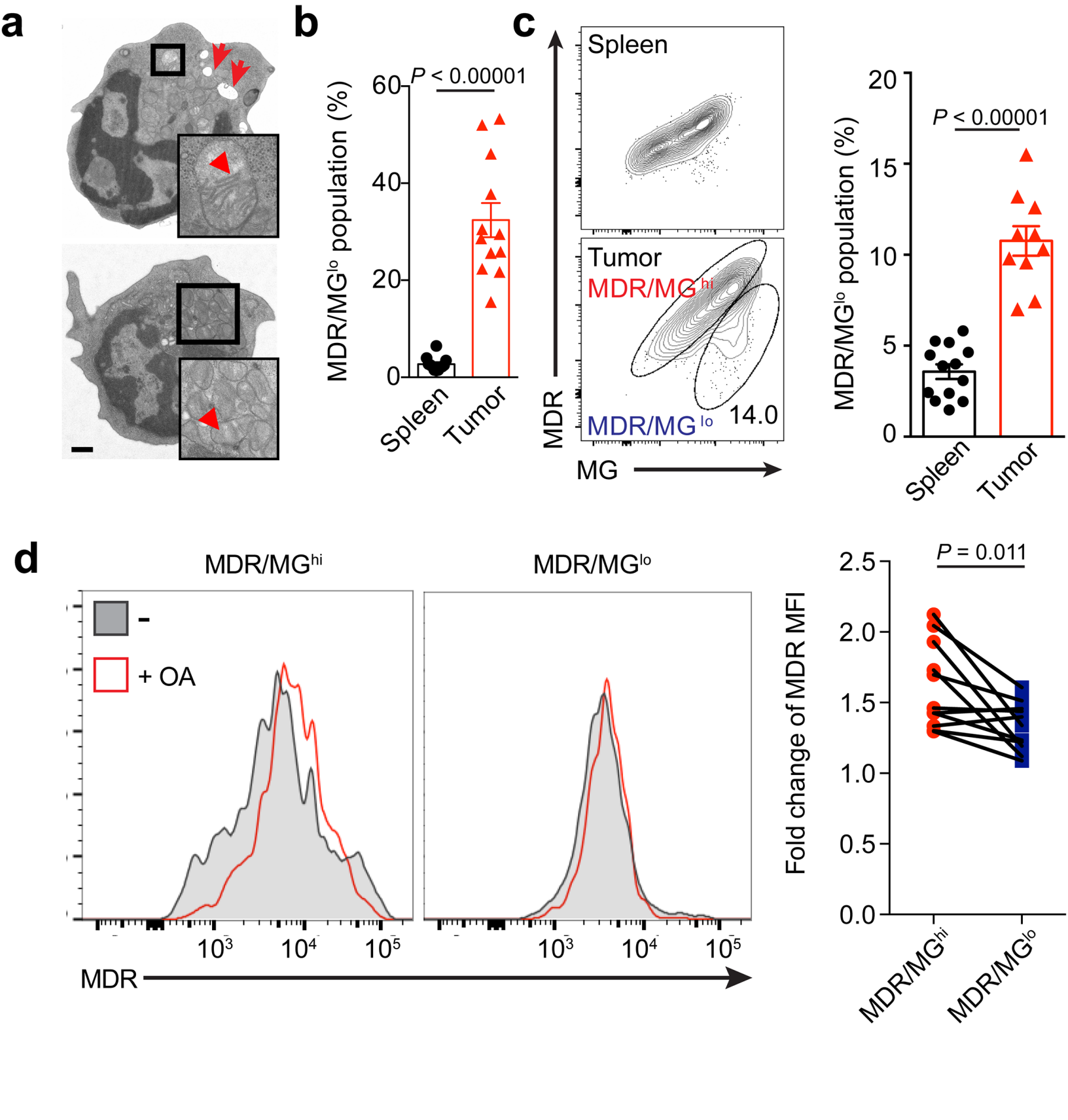

Extended Data Figure 2

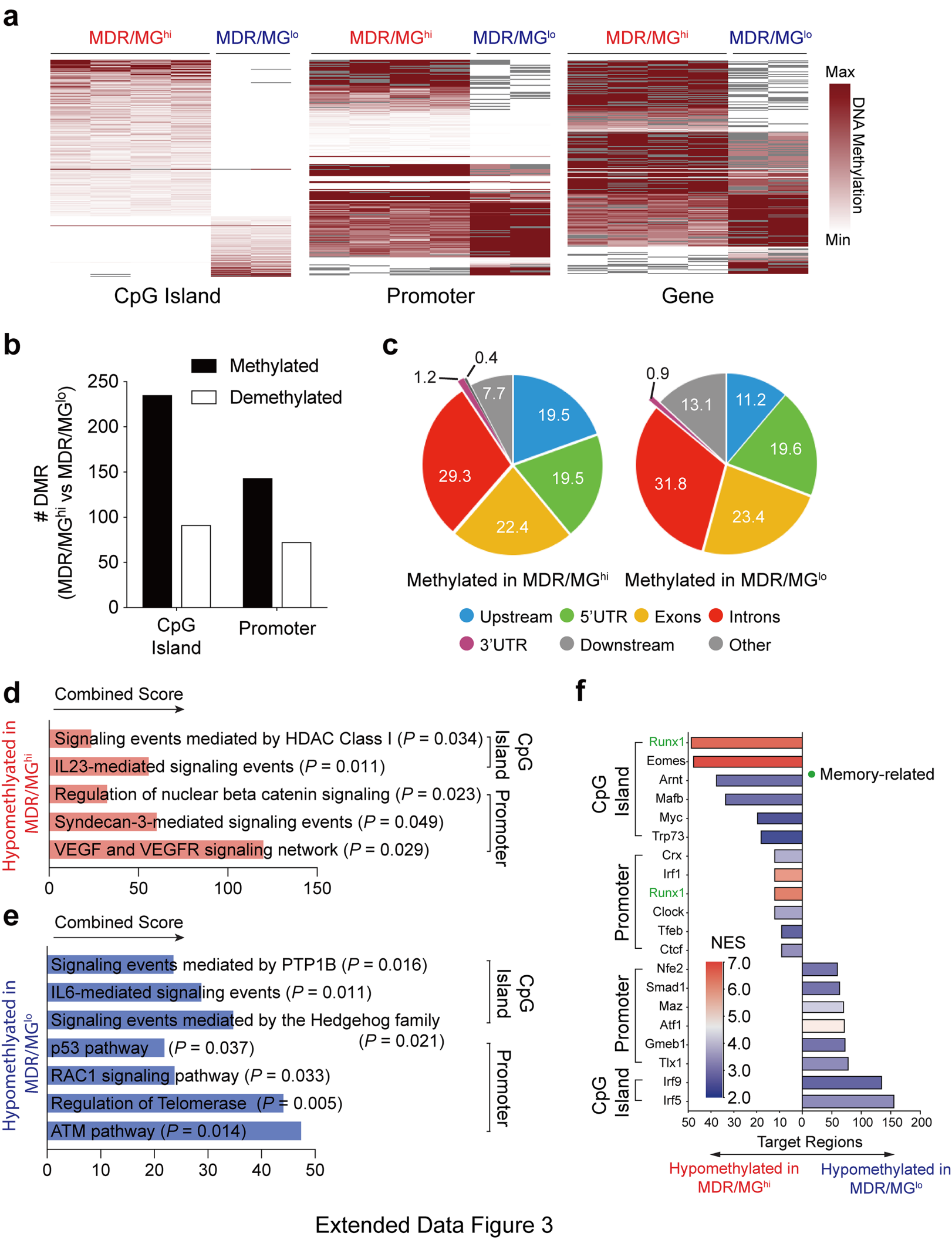

Extended Data Figure 3

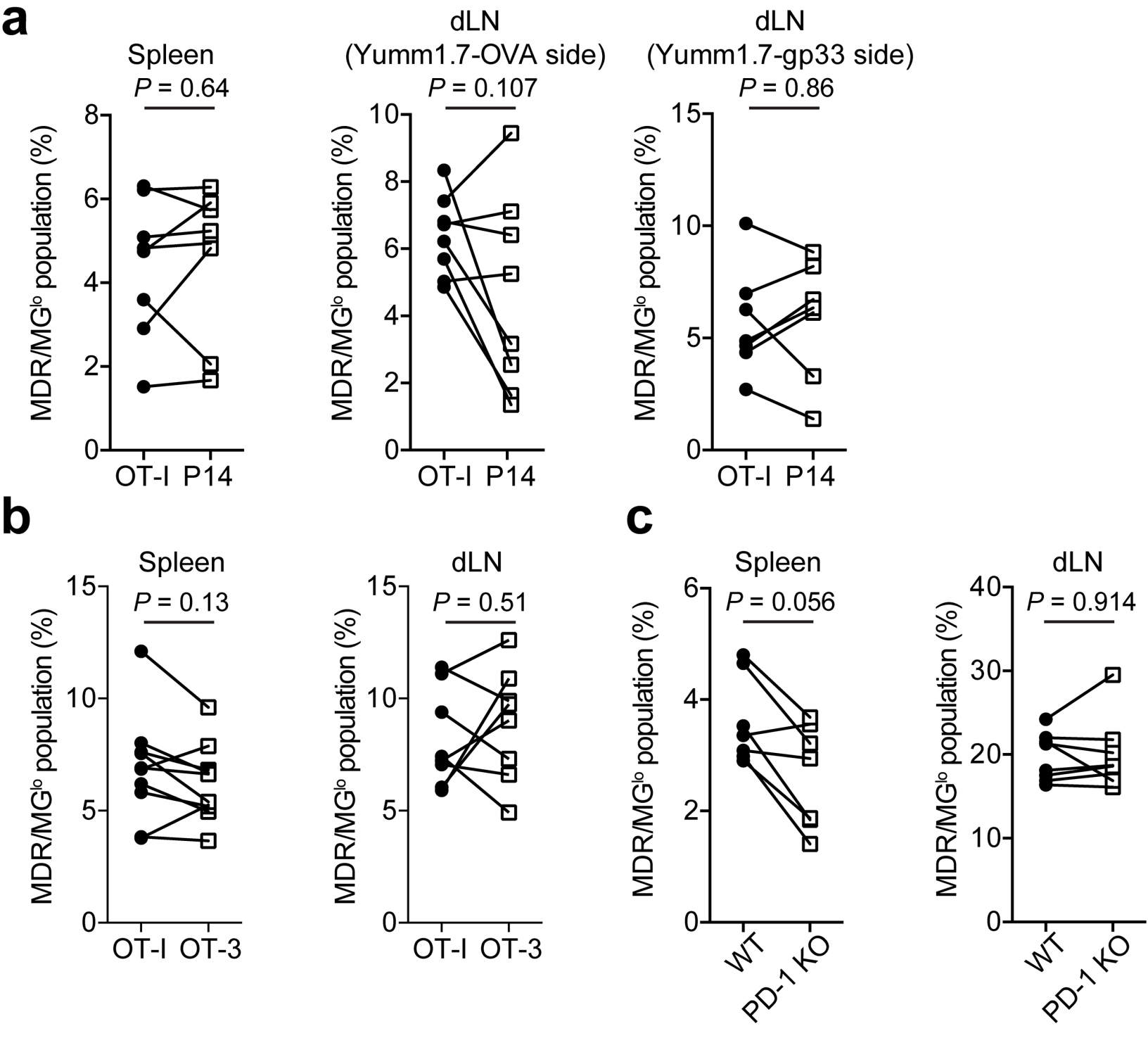

Extended Data Figure 4

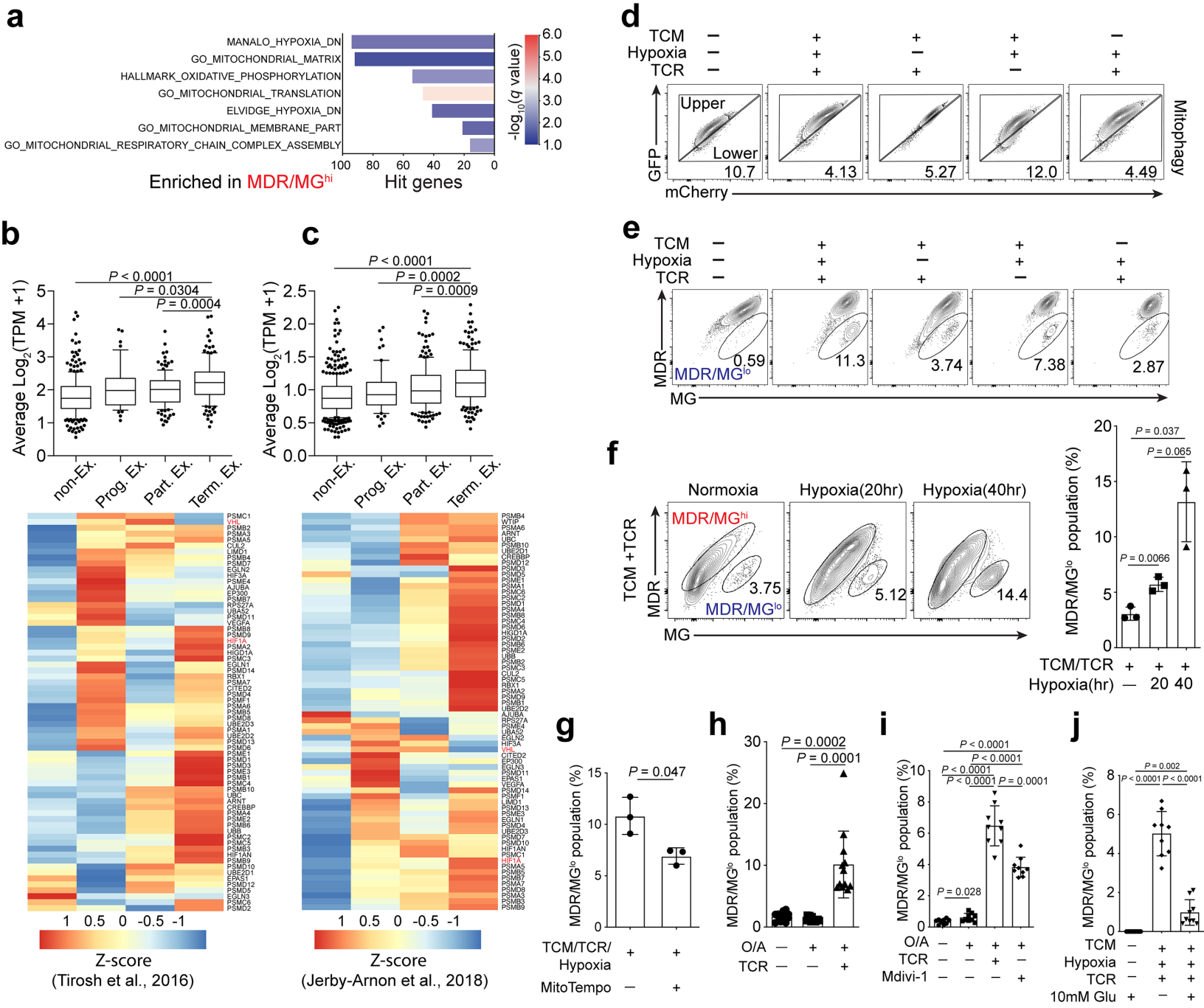

Extended Data Figure 5

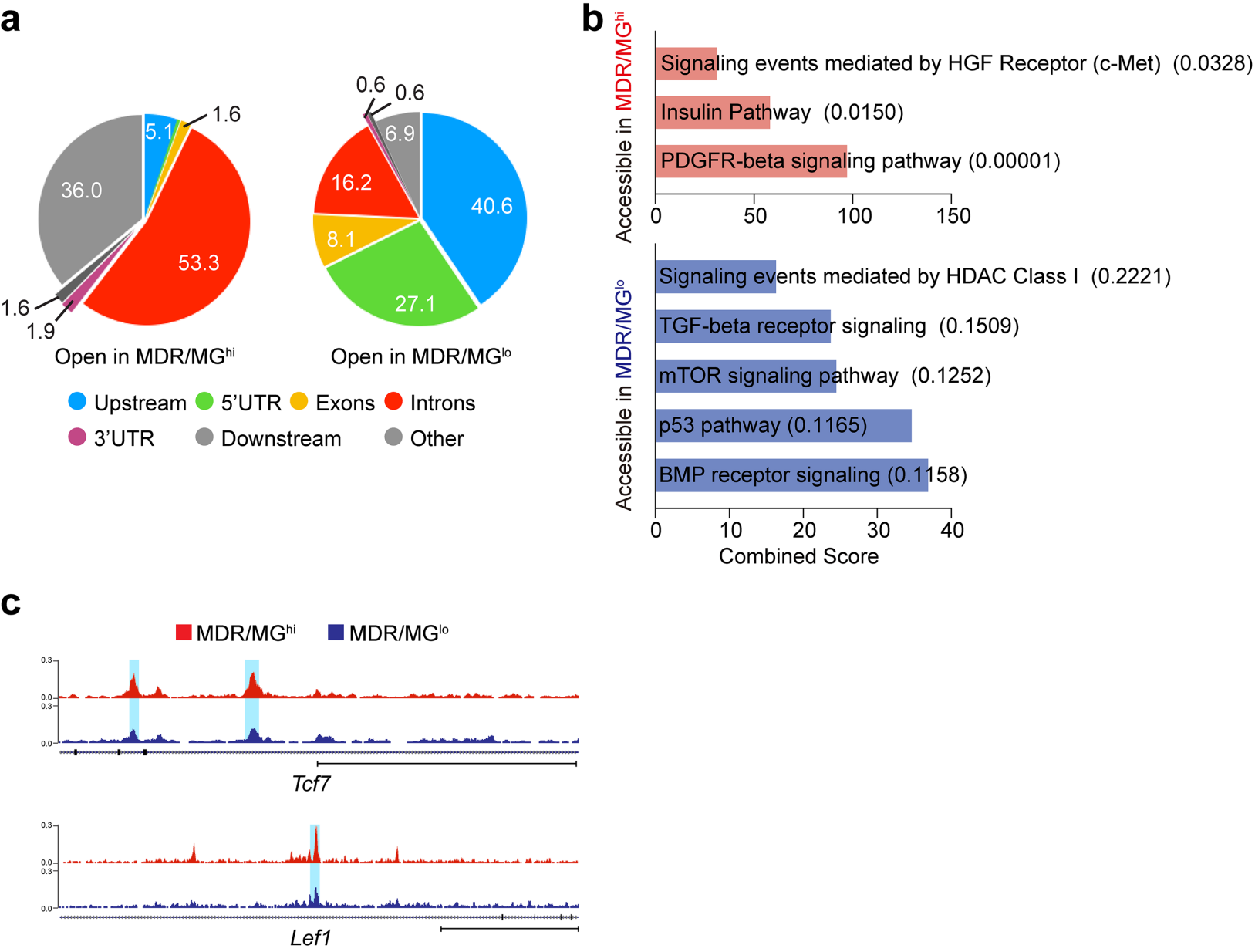

Extended Data Figure 6

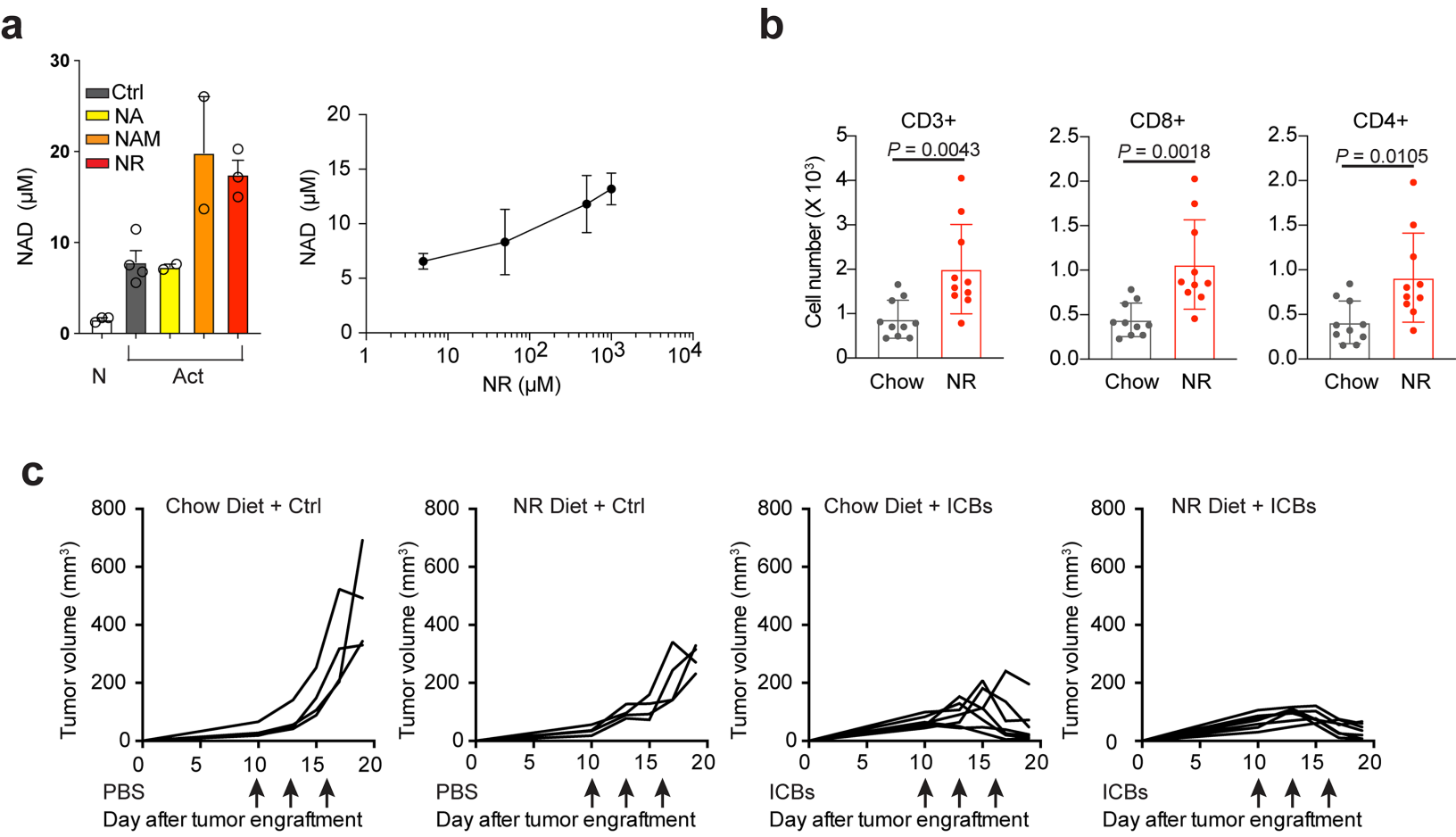

Extended Data Figure 7